Ni/CeO2 Nanoparticles Promoted by Yttrium Doping as Catalysts for CO2 Methanation

Valeria La Parola, Chao Sun, Patricia Beaunier, Leonarda F Liotta, Patrick da Costa

Ni/CeO_2 Nanoparticles Promoted by Yttrium Doping as Catalysts for CO_2 Methanation

Chao Sun [a], Patricia Beaunier [b],Valeria La Parola [c],Leonarda F. Liotta [c,*], Patrick Da Costa [a,*]

[a]Sorbonne Université, CNRS UMR 7190, Institut Jean Le Rond d'Alembert, F-78210, Saint-Cyr-l'École, France

[b]Sorbonne Université, CNRS UMR 7197, Laboratoire de Réactivité de Surface, 75005, Paris, France

[c]Institute for The Study of Nanostructured Materials (ISMN)-CNR, Palermo 90146, Italy

* patrick.da_costa@sorbonne-universite.fr; *leonardafrancesca.liotta@cnr.it

Abstract:

Ni (5 wt.%) catalysts over yttrium modified CeO_2 oxides synthesized by hydrothermal method were prepared. For comparison Ni was supported over pure CeO_2 and Y_2O_3. Characterizations by N_2 adsorption/desorption, XRD, XPS, TEM/HRTEM, H_2-TPR, CO_2-TPD and TGA were carried out. The catalytic performance in CO_2 methanation reaction were tested between 200-450 °C, under atmospheric pressure, at WHSV of 60,000 $h^{-1} \cdot g_{cat}^{-1}$ and reactant molar ratio of $CO_2/H_2/Ar$=15/60/25. Steady-state tests were carried out at 300 °C for 7 h over selected catalysts.

Doping CeO_2 with Y promotes the decrease of the particle size of CeO_2 and the formation of CeO_2 nanorods, increases the specific surface area and the number of oxygen vacancies, enhances the metal-support interaction with respect to the un-promoted Ni/CeO_2. The methanation results showed that the 2 wt.% Y modified Ni/CeO_2 catalyst exhibited the best CO_2 conversion and high selectivity towards methane.

Keywords: CO_2 methanation, Ni/CeO_2, yttrium promotion, oxygen vacancies, metal-support interaction.

1. Introduction

The concentration of carbon dioxide (CO_2) in the atmosphere has been growing since the industrial revolution causing many environmental issues, such as ocean acidification, extreme climate, rise of sea level, which makes the utilization of CO_2 necessary in the next years.[1–4] Several routes have been already established for the CO_2removal, e.g. sequestration, physical storage and chemical usage.[3] Among these methods, the CO_2 chemical conversion was considered as the most feasible way, because it not only produces high-valued chemicals, but also contributes to reduce the emissions of CO_2.[3]

Many studies have been focused on the CO_2 chemical recycling, such as CO_2 dry reforming of methane, CO_2 hydrogenation to produce methanol, formic acid, diethyl ether and methane.[3,5] Among these methods, CO_2 methanation, also called Sabatier's reaction ($CO_2 + 4H_2 = CH_4 + 2H_2O$), was regarded as the most potential way for CO_2 utilization because of its high activity and moderate reaction condition, making it possible in commercial production.[3,6] The methanation, involving CO_2reaction with hydrogen produced by water electrolysis, can be used to transform excess electricity coming from unstable renewable energy (e.g. hydropower, wind energy or solar power) to methane or synthetic natural gas (SNG).[2,7] Also, the methane produced from this power-to-gas (PtG) route can be directly inserted into the existed infrastructure for transportation or storage.

Considering the benefits of CO_2 methanation, numerous efforts have been devoted over the last decades to the research in this topic and most publications reported on noble

metals and transition metal-based catalysts e.g., Pd,[8] Ru,[9] Rh,[10] Fe,[11] Co,[11,12] Ni.[13–16] So far, the noble metal catalysts, like Ru and Rh have been reported as effective in CO_2 methanation with the highest selectivity towards CH_4 in CO_2 methanation.[10,17] However, noble metals were not appropriate for industrialized production because of their high cost and sintering at high temperature, limiting large-scale application.

Among the non-noble metal catalysts, Ni catalysts supported on various oxides become good alternatives for methanation reaction thanks to their benefits of relatively high catalytic activity, low cost and high availability.[6] Supports with high surface area, appropriate basicity and strong metal-support interaction, play an important role in enhancing CO_2 conversion and selectivity towards CH_4. Various supports have already been studied for nickel-based catalysts, such as SiO_2,[18] α-Al_2O_3,[19] ZrO_2,[20] hydrotalcite based supports,[14–16,21] MgO,[22] TiO_2,[23] mesoporous oxides,[24–27] CeO_2 and Y_2O_3.[13,28–31]

CeO_2 had attracted plenty of interests because of its unique redox property. It can create oxygen vacancies during the redox process Ce (III)/Ce (IV), promoting the activation of CO_2.[32] Tada et al.[33] reported that Ni/CeO_2 catalysts showed higher CO_2 conversion and CH_4 selectivity at low temperatures compared to Ni catalysts supported on α-Al_2O_3, TiO_2 and MgO. Such effect was attributed to the formation of oxygen vacancies on the surface of partially reduced CeO_2, promoting the activation of CO_2 and adsorption of CO_2 derivatives. Zhou et al.[34] prepared CeO_2 with different structures and used the synthesized CeO_2 as support to prepare Ni/CeO_2 catalysts. The characterization results revealed that the CeO_2 (NCT) prepared by hard-plate method supported Ni catalyst possessed well-ordered mesoporous structure, high specific surface area, strong metal-support interaction, smaller Ni^0 particle size and higher dispersion of active species

than Ni catalysts supported over CeO_2 with different structures, thus showing the highest CO_2 conversion, 100 % of CH_4 selectivity, and good stability at T =340 °C. The study of the CO_2 methanation mechanism over Ni/CeO_2 and Ni/Al_2O_3 catalysts revealed that the high methanation activity and selectivity of Ni/CeO_2 were attributed to the presence of active sites at the nickel-ceria interface for CO_2 adsorption and dissociation, while dispersed metallic Ni particles activated H_2, thus, the combined effect of two types of active sites led to the high activity and selectivity.[35] Thus, Ni/CeO_2 based catalysts being able to chemisorb and dissociate CO_2 have been widely investigated in CO_2 methantion.

Although several reports claim Ni/CeO_2 as a potential catalyst for methanation, the catalytic stability with time on stream is still a brake to its industrialization due to the occurrence of side-reactions. Many efforts have been devoted to improve the Ni/CeO_2 catalysts e.g., tailoring the structure of CeO_2,[36,37] novel preparation method,[22] doping the catalyst with promoters.[38] Yu et al.[30] added in the preparation of Ni/CeO_2 nanoparticles g-C_3N_4 as a sacrificial and protective template. Several characterization methods used in order to investigate such catalysts, revealed enhanced interaction between Ni and CeO_2 and decreased Ni particle size on the modified catalyst, thus facilitating the adsorption and dissociation of the reactants with higher methanation activity and CH_4 selectivity.

Bian et al.[37] prepared Ni/CeO_2 catalysts with tunable CeO_2 structure i.e. ceria nanorods (NR) and ceria nanocubes (NC) and investigated their catalytic performance in CO_2 methanation. Among the prepared catalysts, the Ni/CeO_2 (NR) exhibited higher conversion and selectivity towards CH_4 at low temperature, which was attributed to the higher concentration of Ce^{3+} on the surface.

Yttrium has been reported to be an effective promoter on nickel catalysts for

various CO_2 utilization reactions, because it enhances the redox properties of nickel, increases the specific surface area and promote weak and medium basic sites in comparison with non-modified samples.[39,40] Moreover, yttrium has been proven to result in the formation of Y_2O_3-ZrO_2 solid solution for Ni-based hydrotalcite-derived catalyst and enhance the stability of catalysts at high temperature during TOS test of DRM reaction.[41] Takano et al.[42] studied the effect of Y molar ratio on Ni/ZrO_2 catalyst for CO_2 methanation and found that the doping of yttrium could promote the formation of t-ZrO_2 and c-ZrO_2 phases when Y/(Y+Zr) ratio was not exceeding 0.333, resulting in the formation of oxygen vacancies over t-ZrO_2 and/or c-ZrO_2 phases compared to yttrium-free catalyst, thus showed better activity in CO_2 methanation.

To the best of our knowledge, until now, no research concerning the effect of yttrium loading on the morphology, structure, and oxygen mobility of Ni/CeO_2 catalysts for CO_2 methanation has been reported.

In the present study, Ni nanoparticle catalysts supported on yttrium-modified CeO_2 nanoparticle prepared by hydrothermal method were studied in CO_2 methanation. The aim of the present work is to investigate the relationship between the modification induced by yttrium promotion on the physico-chemical properties and catalytic performances of Ni/CeO_2 catalysts. For this purpose, the catalysts as calcined, reduced or spent (after methanation test or steady-state test) samples were characterized by XRD, TEM, H_2-TPR, CO_2-TPD, N_2 adsorption-desorption, XPS and TGA techniques. The structure-activity relation was discussed.

2. Experimental

2.1. Catalysts preparation

The catalysts were synthesized by a two steps method. First, CeO_2, Y_2O_3, and yttrium-promoted CeO_2 (denoted as CeO_2-YX%) supports were prepared by hydrothermal method. In a typical procedure, 6 g of cerium nitrate, $Ce(NO_3)_3 \cdot 6H_2O$ (Aldrich, 99%) and an appropriate amount of yttrium nitrate hexahydrate, $Y(NO_3)_3 \cdot 6H_2O$, (Aldrich, 99%) were dissolved in 30 mL of H_2O, then, 40 mL of NaOH (2.5 mol L^{-1}; Aldrich, >98%) were added to the solution under vigorous stirring. The resulting suspension was rapidly transferred into a 100 mL Teflon autoclave and heated in an oven at 120 °C for 24 h. After aging, the obtained precipitate was filtered and washed with deionized water until neutral pH. The resulting powder was dried at 80 °C overnight and calcined at 550 °C for 5 h in static air with a heating rate of 2 °C/min. The Y loadings with respect to CeO_2 are 0.5, 1.0, 2.0, 5.0 weight percent, respectively.

CeO_2 and Y_2O_3 pure oxides were prepared by the same method, starting from $Ce(NO_3)_3 \cdot 6H_2O$ (Aldrich, 99%) or $Y(NO_3)_3 \cdot 6H_2O$ precursors.

The nickel catalysts were synthesized by wetness impregnation method of the so prepared supports with an aqueous solution of $Ni(NO_3)_2 \cdot 6H_2O$. After the impregnation process, the solids were dried at 100 °C overnight and calcined at 550 °C for 5 h with a heating rate of 2 °C/min. The nickel loading for all the samples is 5 wt%. The resulting catalysts were labeled according to the weight loading of Ni and Y, i.e., 5Ni/CeO_2, 5Ni/Y_2O_3, 5Ni/CeO_2-Y0.5%, 5Ni/CeO_2-Y1.0%, 5Ni/CeO_2-Y2.0% and 5Ni/CeO_2-Y5.0%.

2.2. Catalysts characterization

Elemental analysis of the catalysts was carried out using a X-ray fluorescence wave-dispersive spectrometer (XRF 1800 Shimadzu).

The specific surface areas (SSA), pore volume and pore size of the materials were measured by N_2 adsorption-desorption isotherms using a Micromeritics ASAP2020system. Before analysis, the samples were degassed in vacuum at 250 °C for 2 h, then the measurement was performed at liquid nitrogen temperature (-196 °C). The Brunauer–Emmett–Teller (BET) method was used to calculate the SSA. The BJH method was applied to estimate the pore volume and average pore size.

The crystalline structure of calcined, reduced and spent samples was determined by Powder X-ray diffraction patterns (XRD), performed on a Bruker D5000 diffractometer equipped with a Cu Kα anode and graphite monochromator. The data were recorded in a 2θ range of 10°-80° or 20°-80° (depending on the crystalline nature of the samples) with a step size of 0.05° and time per step of 5 s. The crystalline phases of samples were analyzed according to ICSD files (Inorganic Crystal Structure Database). The mean crystallite size was calculated by the Debye-Scherrer equation shown in Eq. (1).

$$D = \frac{0.9\lambda}{B\cos\theta} \qquad \text{Eq. (1)}$$

where D represents the average crystalline size, 0.9 is the Scherrer parameter, λ is the wavelength of the X-ray radiation (0.15406 nm), B denotes the full width at half maximum of the peak (FWHM), and θ is the angular position of the peak.

The reducibility of the catalysts was evaluated by temperature-programmed reduction (H_2-TPR) measurements. The experiments were carried out in a Micromeritics Autochem 2950HP apparatus equipped with a thermal conductivity detector (TCD). Prior

to TPR procedure, the samples (125 mg) were pretreated with the gas mixture 5% O_2/He (50 mL/min) at 350 °C for 30 minutes, then the furnace was cooled down to room temperature under pure He flow. After pretreatment, the samples were heated from ambient temperature to 1050 °C with a heating rate of 10 °C/min under the gas mixture of 5 % H_2/Ar (30 mL/min). The H_2 consumption values were calculated, with a precision of ±10%, by integration of the TPR curves registered by TCD through a calibration procedure. On the basis of H_2 consumption in the α peak, the oxygen vacancy content (%), V_0 (%) was calculated according to the Eq. (2):

$$V_0(\%)=\frac{(\text{mmol } O2-/\text{gcat})}{(\text{total mmol } O2-/\text{gcat})} *100 \qquad \text{Eq. (2)}$$

where the mmol O^{2-}/g_{cat} correspond to the mmol of H_2/g_{cat} from α peak and the total mmol O^{2-}/g_{cat} where calculated on the basis of CeO_2 or CeO_2-Y content/g_{cat}).

The basicity of catalysts was investigated through CO_2 temperature-programmed desorption (CO_2-TPD) carried out in a BEL-M instrument (BEL Japan Inc.) equipped with a thermal conductivity detector (TCD). Prior to adsorption, the samples (60 mg) were reduced under 5 %H_2/Ar flow (50 mL/min) at 550 °C. Then, the furnace was cooled down to 80 °C under the same condition, following pretreatment under pure He (50 mL/min) for 15 min. Afterwards, the adsorption of CO_2 was performed in CO_2 mixture (10 % CO_2/He, 50 mL/min) for 1 h, then, pure He was then used to remove the physically adsorbed CO_2 for 30 min at 80 °C. Finally, the temperature-programmed desorption procedure was carried out from 80 °C to 550 °C with a heating rate of 10 °C/min under pure He flow of 50 mL/min.

Transmission electron microscopy (TEM) and Energy Dispersive X-ray spectroscopy (EDX) analyses were carried out with JEM-2010 and JEM-2100Plus (JEOL,

Tokyo, Japan) transmission electron microscopes operating at 200 kV for the reduced catalysts. Before measurement, the reduced samples (reduction condition: 550 °C for 1 h in 5 % H_2/Ar) were dispersed in ethanol, following the suspension being added dropwise on a copper grid covering with carbon film, then the prepared materials were used for the microscopy measurement.

The X-ray photoelectron spectroscopy (XPS) measurements were performed with a VG Microtech ESCA 3000Multilab spectrometer, equipped with a dual Mg/Al anode, with an excitation source of unmonochromatized Al Kα radiation (1486.6 eV). The sample powders as received (calcined samples and samples after steady state test) were analyzed as pellets, mounted on a double-sided adhesive tape. The pressure in the analysis chamber was in the range of 10^{-8} Torr during data collection. The constant charging of the samples was removed by referencing all the energies to the $Ce3d_{5/2}$ component at 882.1eV. Quick scans of Ce3d region were performed before each analysis in order to evaluate possible reduction under the beam. Analyses of the peaks were performed with the software CasaXPS. Atomic concentrations were calculated from peak intensity using the sensitivity factors provided by the software. The binding energy values are quoted with a precision of ±0.15 eV and the atomic percentage with a precision of ±10%.

The thermogravimetric analyses (TGA) of the CeO_2-Y supported catalysts,previuosly reduced at 550 °C for 1 h, were performed in a TGA/DSC1 STAR System from Mettler Toledo Inc. The sample of 15 mg was pretreated in N_2 (30 mL/min) from 25 °C to 500 °C with a heating rate of 10 °C/min, holding time at 500 °C for 15 min, then, it was cooled down under N_2 atmosphere to 150 °C. At 150 °C, the sample was

satured with pure O_2 (30mL/min) during 1 h and cooled to 25 °C still under O_2. Finally, the sample was heated, under N_2 (30 mL/min), from room temperature up to 600 °C (ramp rate 5 °C/min), thus, the removal of physi- and chemisorbed oxygen species occurred and the weight loss was taken into account in order to evaluate the surface oxygen vacancies content of the sample. Each experiment was repeated 3 times in order to check the reproducibility.The gases flowing duringthe above steps were monitored by on line mass quadrupole (ThermostarTM, Balzers).

2.3. Catalytic test in CO_2 methanation reaction

The catalytic performances of the catalysts in CO_2 methanation reaction were investigated in a quartz U-type tubular reactor (8mm inner diameter) at atmospheric pressure heated through electrical furnace, using a K-type thermocouple placed closed to the catalytic bed to monitor the temperature of catalyst bed. Prior to reaction, the sample (100 mg) was reduced in 5 % H_2/Ar (100 mL/min) at 550 °C for 1 h with a heating rate of 5 °C/min. After cooling down to 200 °C, the reactant gas mixture,100 mL/min, with molar ratio of $CO_2/H_2/Ar$=15/60/25 was fed into the catalyst (WHSV=60,000 mL $h^{-1}g_{cat}^{-1}$). The products of outlet were analyzed by an online gas micro chromatograph (490 Varian, Agilent) and the flow rates of inlet and outlet were also measured by flowmeter. The tests were carried out from 200 °C to 450 °C (increasing the temperature step by step of 50 °C), waiting 30 minutes at each temperature for obtaining steady state values. Considering that only CH_4 and CO were registered as products in the outlet mixture, the CO_2 conversion and CH_4 selectivity were calculated according to the Eq.(3) and Eq.(4):

$$X_{CO2}\ (\%)=\frac{[CO2]in-[CO2]out}{[CO2]in}*100=\frac{\%CO2in.Qin-\%CO2out.Qout}{\%CO2in.Qin}*100 \qquad \text{Eq.(3)}$$

$$S_{CH4}\ (\%)=\frac{[CH4]out}{[CH4]out+[CO]out}*100=\frac{\%CH4out.Qout}{\%CH4out.Qout+\%COout.Qout}*100 \qquad \text{Eq.(4)}$$

In which, X is the CO_2 conversion of reactants; S represents the selectivity of CH_4; Q is the flow rate (in for inlet, out for outlet); $[CO_2]_{in}$ and $[CO_2]_{out}$ are the molar quantities of inlet and outlet, respectively; $[CH_4]$out and [CO]out represent the molar quantities of CH_4 and CO in outlet, respectively**.** The calculated values consider an experimental error estimated at ± 5 %.

2.4. Steady-state tests of Ni/CeO₂ based catalysts in CO₂ methanation reaction

The steady state tests were performed on three selected Ni catalysts, by using the same set-up previously described, for evaluating the stability of CO_2 conversion and selectivity towards CH_4. In a typical process, 100 mg of calcined sample was loaded into the reactor. After reduction, the sample was cooled down to 300 °C, then the gas mixture with molar ratio $CO_2/H_2/Ar$=15/60/25 (100 mL/min) was fed into the catalyst (WHSV=60,000 mL $h^{-1}g_{cat}^{-1}$). The products were analyzed by the TCD detector in GC (490 Varian, Agilent). The experiment was maintained at 300 °C for 7 h.

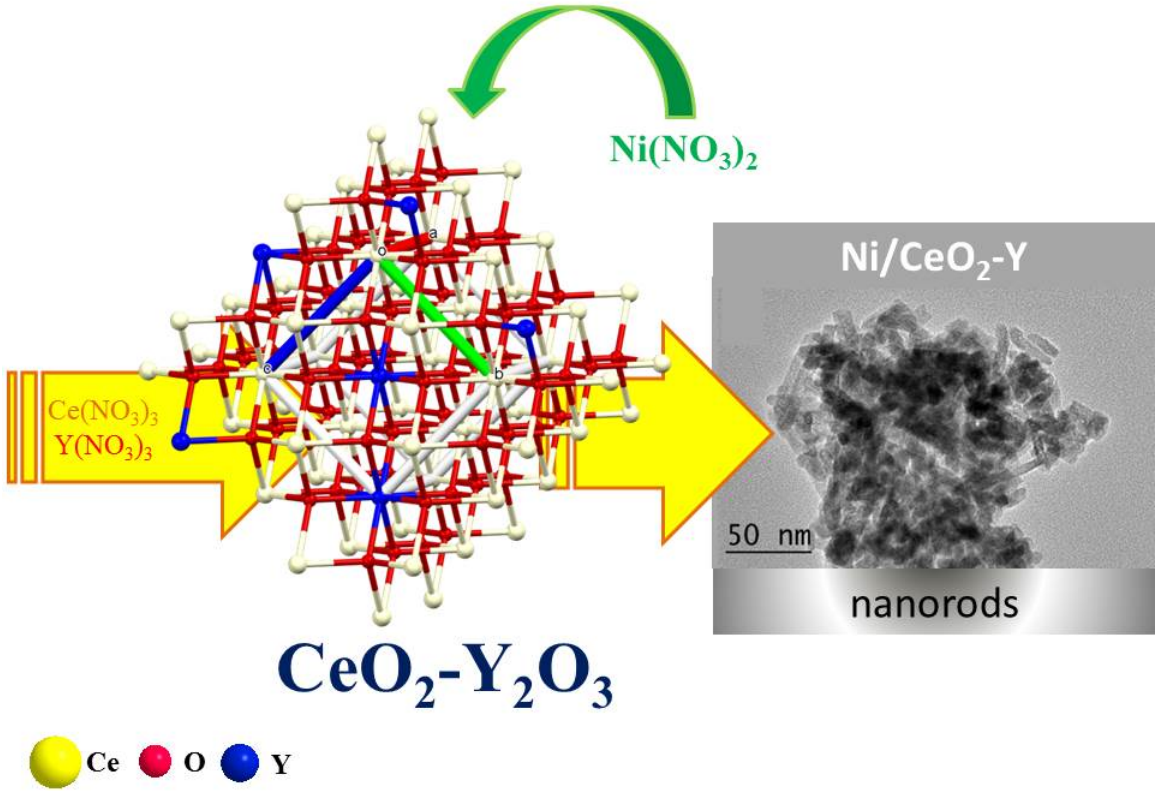

Scheme 1. Chemical Composition and Structure of a Typical Ni/Ce_{O2}−Y Catalyst

3. Results and discussion

3.1. Catalysts characterization

3.1.1 Textural properties, structural parameters and chemical vs surface compositions of the catalysts

As determined by XRF analyses, the real loading of Ni and Y in the prepared catalysts was equal to the nominal one ±10%. In **Table SI 1**, the XRF derived chemical composition is listed. The textural properties of the supports and calcined catalysts were

measured by N_2 adsorption/desorption technique. The specific surface areas (SSA), pore volume and average pore size of the supports and catalysts are displayed in **Table SI2** and **Table SI3**. It results that the SSA, pore volume and pore diameter values of Y-modified supports increase with the increase of yttrium loading from 0.5 to 5.0 wt.% of Y. A similar trend was registered for the Ni supported catalysts showing the best textural properties in the case of 5Ni/CeO_2-Y2.0% that was characterized by SSA of 78.9 m^2/g, pore volume equal to 0.29 cm^3/g and pore diameter of 12.9 nm. Slightly lower surface area and porosity values were registered for the Ni catalyst with 5 wt.% of Y. By comparing **Table SI3** and **Table SI2**, it results that after Ni deposition and further calcination, SSA and porosity values generally decrease, although at the highest Y content (2 and 5 Y%) the morphological properties appear less affected, suggesting a beneficial effect of Y doping, especially for Y 2 wt%. It is noteworthy that Y_2O_3 is characterized by higher SSA and pore volume with respect to the undoped CeO_2 but suffers significant shrinkage after Ni deposition, likely due to the presence of small pores of 4.7 nm that easily merge in larger and less deep pores. Positive effects induced by yttrium on the textural properties of different types of supports were also reported in the literature.[39,43,44] Świrket al.[43] studied the effect of Y on Ni-based double layered hydroxides for dry reforming of methane and found that doping Y inside the matrix promotes the increase of specific surface area. Similar results were also found for Ce and Y modified double layered hydroxides, showing that higher SSA, pore volume and pore size were obtained over Y-modified catalyst compared to those of Ce-promoted material without the presence of Y.[45]

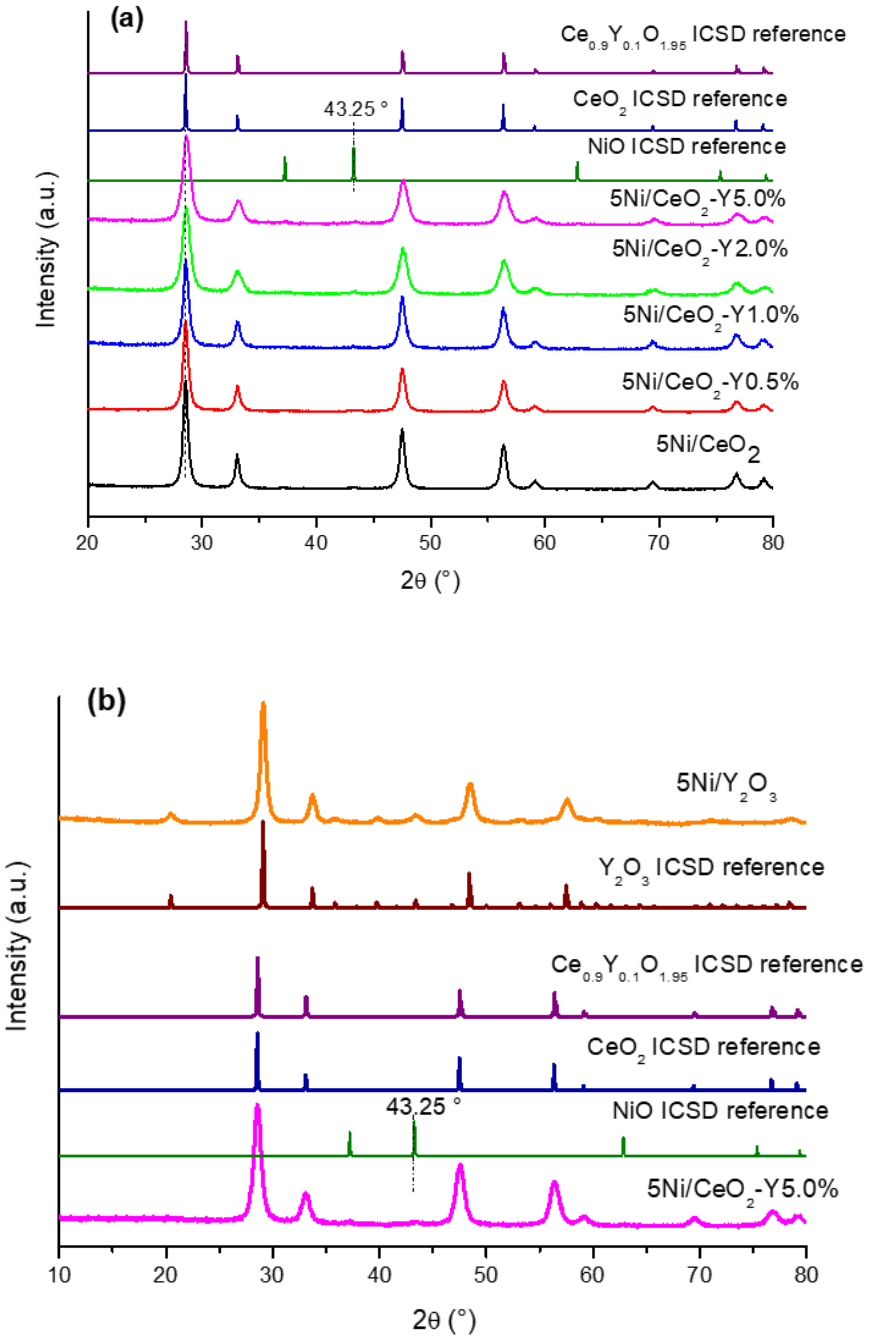

Fig. 1 a,b XRD patterns of the catalysts calcined at 550 °C for 5 h : (a) Ni/CeO_2 and $NiCeO_2$-Y(0.5-5%) catalysts; (b) Ni/Y_2O_3 and Ni/CeO_2-Y5%. The reference ICSD files are also displayed.

In order to investigate the structural properties of the catalysts, XRD measurements

were registered for calcined, reduced and spent samples. The XRD patterns are presented in **Fig. 1a,b** and **Fig. 2a,b** for calcined and reduced catalysts, respectively, along with the ICSD reference patterns of NiO (no. 24018) , metallic Ni (no. 41508), CeO_2 (no. 28753), Y_2O_3 (no. 193377) and $Ce_{0.9}Y_{0.1}O_{1.95}$ (no. 28808) solid solution. Depending on the nature of catalysts and on the treatment, different angular ranges are displayed. From **Fig. 1a,b**, distinct diffraction peaks of CeO_2 were found for all the catalysts, while signals of Y_2O_3 crystalline phase were detected only for the Ni/Y_2O_3 sample. In **Fig. 1b** the diffraction pattern of Ni/CeO_2-Y 5.0% was plotted for comparison in order to exclude any segregation of yttria phase. No features at 2θ=43.25° corresponding to nickel oxide (NiO) were detected, suggesting high dispersion of nickel species. As for Y-modified CeO_2 supported Ni-based catalysts, as it can be seen in **Fig. SI 1a**, where the enlarged patterns in the angular range 27-30° 2θ are reported, the Y doping does not induce any important changes in the CeO_2 structure. The main peaks (111) are all centered between 28.55° 2θ (CeO_2 ICSD reference no. 28753, cubic, space group FM-3M) and 28.57° 2θ ($Ce_{0.9}Y_{0.1}O_{1.95}$ ICSD reference no. 28808, cubic, space group FM-3M)) so it cannot be excluded that at the highest Y loading (5 wt%) possibly a ceria-yttria solid solution is formed. Indeed, thanks to the similar ionic radius some Ce^{4+} ions can be replaced by Y^{3+} with oxygen vacancies formation to compensate the excess negative charge.[44] However, due to the relatively low crystallinity of the samples, no structural refinements were performed. Furthermore, according to ICSD files (references no. 28753 and no. 28808) the structural parameters, d_{111} values, for CeO_2 and $Ce_{0.9}Y_{0.1}O_{1.95}$ references are almost coincident, 3.122 and 3.1207 Å, respectively, so no significant differences are expected in our experimental patterns. On the other hand, if the introduction of Ni^{2+} into the ceria

lattice should occur, a decrease of the lattice parameter of ceria is expected due to its smaller ionic radius (0.69 Å), however, it would generate new oxygen vacancies inducing a small expansion of the cell, so the two effects would cancel out.

Meanwhile, a broadening of the diffraction peaks of CeO_2 was also identified with the increasing dopant of yttrium, as it can be clearly seen from **Fig. SI 1a**. Accordingly, the particle sizes of CeO_2 in calcined catalysts decreased as the increased content of Y, and the smallest size was obtained for 5Ni/CeO_2-Y5% sample (see **Table SI4**). This could partially interpret the increasing SSA and porosity values reported in **Table SI3**. As for Y_2O_3 supported Ni catalyst, it can be affirmed that no distinct diffraction peaks of NiO at 43.25° neither at 37.25° 2θ are detectable even magnifying the patterns (see **Fig. SI 1b** where the NiO reference file is compared with patterns for 5Ni/Y_2O_3 and Y_2O_3 characterized by a peak at 43.39° 2θ).

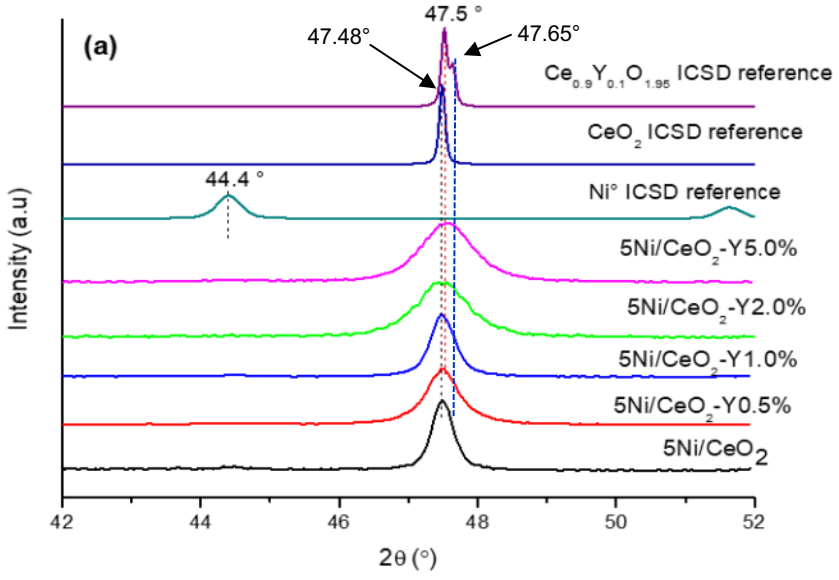

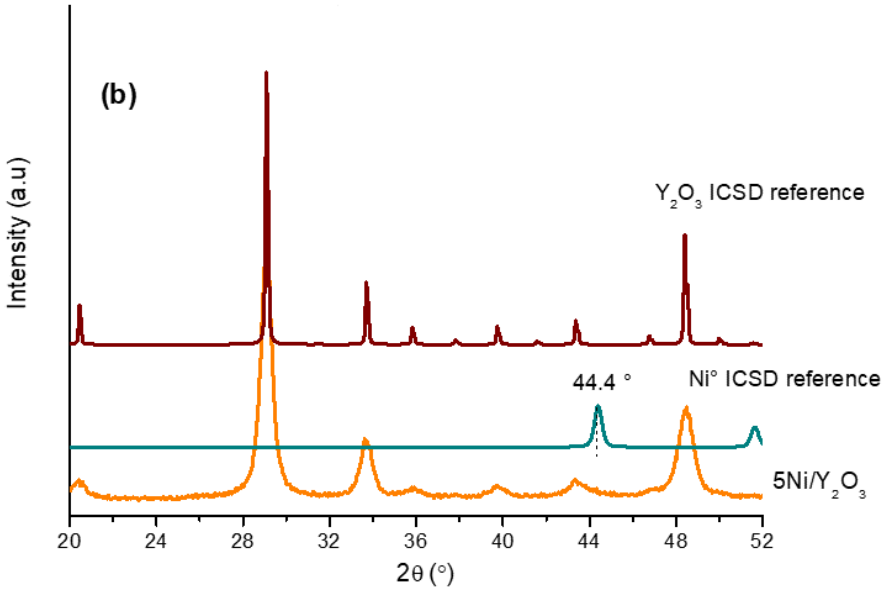

Fig. 2 a,b. XRD patterns of the catalysts reduced at 550 °C for 1 h in the gas mixture 5% H_2/Ar (100 mL/min).

The XRD patterns of the reduced catalysts are presented in **Fig. 2a,b** where the enlarged ranges from 42 to 52 and from 20 to 52° 2θ are displayed for Ni/CeO_2, Ni/CeO_2-Y (0.5-5%) and for Ni/Y_2O_3, respectively, along with the ICSD reference files. Such angular ranges were chosen in order to detect any features ascribable to metallic Ni. No diffraction peaks of metallic nickel at 44.4 °2θ are detectable in any case which means that the active nickel metals keep highly dispersed on the supports after reduction. The (202) peaks of CeO_2 and CeO_2-Y oxides are all centered between 47.48 and 47.65 ° 2θ with an evident broadening of peaks at high Y content, confirming what previously observed for the calcined catalysts (**Fig. 1a** and **Fig. SI 1a**).

For spent catalysts (after methanation reaction) similar features were observed as so far discussed for reduced catalysts, see XRD patterns shown in **Fig.SI 2**. No diffraction

peaks of NiO at 43.25 and at 37.25° 2θ nor of Ni^0 at 44.4° 2θ were detected for Y-modified catalysts, meaning that no sintering of Ni specie (as Ni or as reoxidized NiO) occurs during catalytic test. This finding confirms the high dispersion of nickel species and the occurrence of metal-support interaction stabilizing Ni even after reduction treatment and catalytic test.

The particle sizes of CeO_2, CeO_2-Y and Y_2O_3 were calculated for calcined, reduced and spent catalysts by Debye-Scherrer equation and are listed in the **Table SI4**. The particle size for calcined samples decreases gradually as the increase of Y content, with the smallest size obtained on 5 wt.% Y-modified sample. For the reduced and spent samples, similar trends were also registered by comparing Ni/CeO_2-Y samples at different Y loading, but the smallest particle size of the support was acquired on Ni/CeO_2-Y 2.0%. By comparing the particle size of the support for each catalyst as calcined, reduced or spent, it results that for Ni/CeO_2 the size slightly increased upon reduction or catalytic test, while for Ni/CeO_2-Y and Ni/Y_2O_3 catalysts, the particle sizes were nearly the same.

In brief, the XRD results of calcined, reduced and spent samples indicate that the nickel species keep highly dispersed before/after reaction for all catalysts and the particle sizes of supports decreased due to Y doping. The unaffected structural properties of the catalysts after test illustrate the metal-support interaction in the catalysts, which suppress the sintering of catalyst particles.[29]

The X-ray photoelectron spectroscopy (XPS) analysis performed over calcined

samples was expected to identify the surface compositions and oxidation states of the catalysts. The region of Ce3d, Ni2p, Y3d and O1s of the catalysts were recorded and analyzed by peak fitting procedure. The percentage of Ce (III)/Ce (IV), lattice oxygen (OL)/surface chemisorbed hydroxyl species (OOH), Ni/Ce or Y/Ce, binding energy of O1s, $Ni2p_{3/2}$ and $Y3d_{5/2}$ are listed in **Table SI5**. The survey spectrum and the Y3d, O1s, Ni2p and Ce3d regions of 5Ni/CeO_2-Y2.0% are shown in **Fig. SI3**.

As shown in **Fig. SI3**, the doublet of Y3d with two peaks located at 157.4 eV ($Y3d_{5/2}$) and 159.3 eV ($Y3d_{3/2}$) represents the Y^{3+} species.[46] There is no significant difference regarding to the $Y3d_{5/2}$ position (presented in **Table SI5**) between Y-modified catalysts and pure Y_2O_3 supported catalyst except slight shifts (±0.2 eV), which are in accordance with other reports.[47] The presence of cerium does not influence the position of Y3d peaks, indicating a weak interaction between the two elements. The Y/Ce atomic ratio increase is not linear with the increase of Y content. An uneven distribution of Y between bulk and surface or the presence, in the higher Y content samples, of bigger particles of Y_2O_3 may be responsible for this behavior.

The Ce3d region of 5Ni/CeO_2-Y2.0% shows the typical complex profile, consisted of 10 peaks, which is arisen by the ligand-to-metal charge transfer transitions.[48] Many different approaches deal with the fitting of the Ce3d peak,[49,50] in this study, the approach reported by Burroghs et al.[50] was used, with ten components that take into account the spin orbit splitting of $Ce3d_{5/2}$, $Ce3d_{3/2}$ and others splitting caused by a redistribution of the entire energy spectrum after a core hole is created. There are four components (labeled as v^0, u^0, v^i, u^i) attributed to Ce (III) and six components (labeled as v, u, v^{ii}, u^{ii}, v^{iii}, u^{iii}) attributed to Ce (IV). The data were fitted using the constrains between the

corresponding components $3d_{5/2}$-$3d_{3/2}$ given by Preisler et al.[51]. The Ce (III) percentages calculated as $(Iv^0+Iv^i)/ (Iv^0+Iv^i+Iv+Iv^{ii}+Iv^{iii})*100$, showed in **Table SI5**, ranges between 9 and 19 %, and it can be concluded that the Ce (III) concentration increases with the increasing yttrium content, which was also demonstrated in other literature.[52] The dopant of Y promotes the formation of Ce^{3+}, thus, more oxygen vacancies are created.[53]

The O1s region contained two contributions, one due to lattice oxygen (OL) with BE (Binding Energy) of 529.4 ±0.3 eV,[47,54] the other attributed to the hydroxyl species chemisorbed on the surface (OOH) with BE of 531.5±0.4 eV arising by dissociative adsorption of water.[54–56] As shown in **Table SI5**, the relative amount of OOH increases with increasing Y up to1-2% (within the experimental error) which could be assigned to the increase of Ce^{3+}. Because the oxygen species adsorbed on Ce^{3+} showed higher stability than that of Ce^{4+}.[57] By increasing the amount of yttrium, contribution of the oxygen arising by yttrium oxides segregated on the surface probably occurs and this may give account for the decreases OOH species despite the increase of Ce^{3+}.

The $Ni2p_{3/2}$ profile with a peak centered at 855.0±0.2 eV along with a shake-up peak at 862±0.5 eV is typical of Ni(II).[58] The position at values higher than 853 eV, typical of pure NiO indicates a good interaction between the Ni and the support.[59] The presence of yttrium causes a small decrease (0.2-0.5eV) indicating a moderate modulation of interaction by Yttrium.

Such finding further confirms the occurrence of metal-support interaction in Ni/CeO_2-Y promoted catalysts as argued on the basis of XRD data.

The Ni/Ce atomic ratio decreases with the rise of Y content on the surface of the catalysts, except for Ni/CeO_2-Y1.0%. This fact could be attributed to different factors,

such as slightly bigger Ni particles, a different distribution of Ni on the surface due to changes in morphology or the migration of Ni into the bulk likely forming Ni-Ce-O solid solution. Because XPS analysis is a surface sensitive technique, the ratio between supported metals and bulks support is usually higher than the theoretical ratio. In our case anyway the values of Ni/Ce ratio are quite similar to the theoretical ones. This finding could point out to the presence of big particles, but this hypothesis was discarded on the basis of XRD and HRTEM data, or could be due to a migration of Ni toward the bulk of Ceria (as postulated on the basis of oxygen vacancies). On the contrary Y/Ce ratios are significantly higher than the theoretical values pointing to a surface enrichment of Y. Yttrium surface migration has been found previously in several studies.[59,60] According to Shih et al,[61] the movement of ions may be assisted by diffusion of water and hence can be related to their hydration energy. The hydration energies of Y^{3+} (-3491.1 kJ mol^{-1}) Ce^{3+} (-3370 $kJmol^{-1}$) and Ni^{2+} (2141.8 $kJmol^{-1}$) gives account of the element distribution found in our samples.[61,62]

3.1.2 The reducibility of calcined catalysts

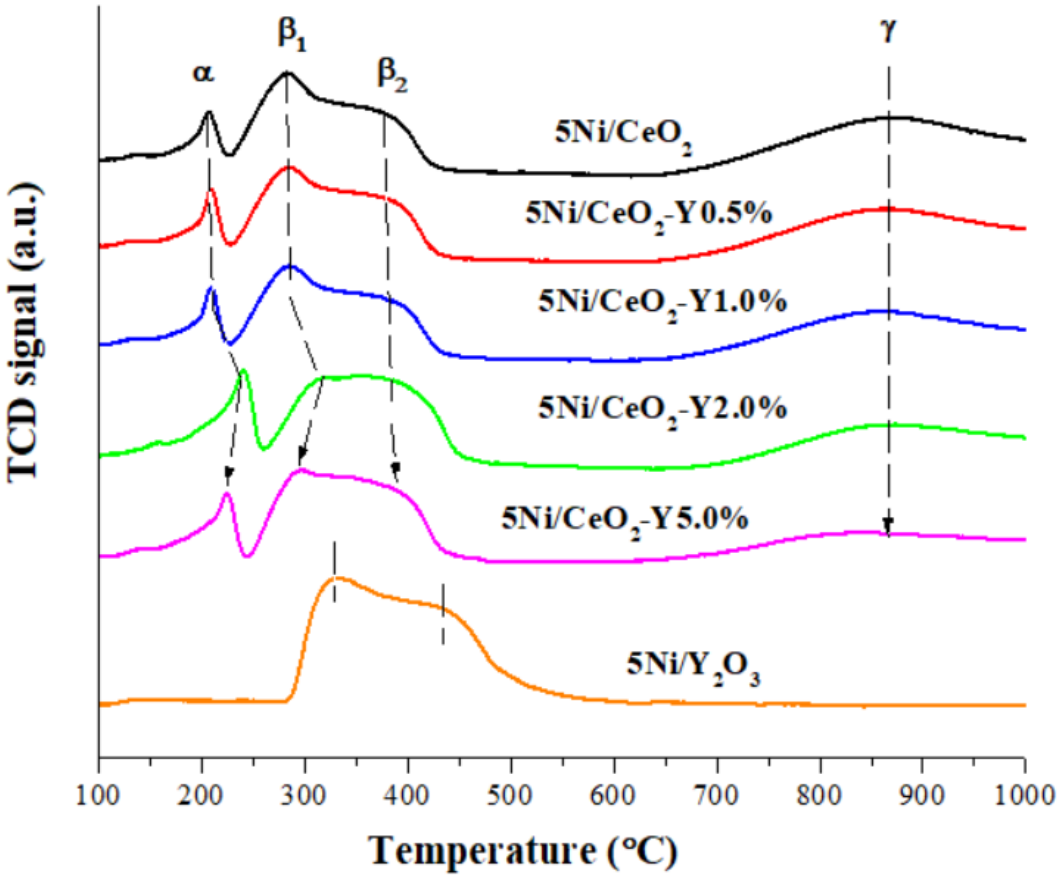

Fig. 3. H_2-TPR profiles; Operating condition: 5% H_2/Ar flow rate of 30 mL/min, ramp of 10 °C/min.

To study the reducibility of the calcined catalysts and determine the optimal reduction condition for CO_2 methanation, temperature-programmed reduction in H_2 (H_2-TPR) was performed on the calcined samples. The H_2-TPR profiles are displayed in **Fig. 3**, the temperatures at the maxima of reduction peaks and H_2 consumption values are listed in **Table 1**. In order to get more insight into the effect of Ni on the reduction properties of the supports, TPR experiments were registered also over selected samples (see **Fig. SI4** and **Table SI 6**). As presented in **Fig. 3**, there are 4 main peaks over Ni/CeO_2 and Ni/CeO_2-Y catalysts, which are labeled as α, β1, β2 and γ in the figure. The

α peak was ascribed to the reduction of oxygen species chemisorbed on the oxygen vacancies that could be generated by partial diffusion of Ni^{2+} or Y^{3+} species into CeO_2 lattice resulting in Ni-Ce-O solid solution or Y-Ce-O solid solution.[30,37,59] It is worth noting that the α peak shifts toward higher temperature with the increase of Y loading until 2 wt.% of Y, and then shifts a little toward lower temperature for the sample with 5 wt.% of Y. Moreover, the H_2 consumption of the α peak (see **Table 1)** gradually increased with Y loading until 2 wt.% of Y, with the highest value. This finding could be explained by an increased concentration on the surface of the catalysts of Ce^{3+} ions able to chemisorb oxygen species reducible below 250 °C (see TGA curves and XPS analysis) and is in agreement with the change of the morphology of Ni/CeO_2-Y catalysts by increasing the Y loading from 0 up to 5wt. % (see TEM characterization).[37] On the other hand, the shift of the α peak toward higher temperature until 2 wt.% of Y and the highest hydrogen consumption registered for such peak, suggest that doping ceria with 2 wt.% of Y produces the highest oxygen vacancy concentration with strongly chemisorbed oxygen. It is worth noting that no α peaks at around 200-250 °C were observed in the TPR profiles of CeO_2 and CeO_2-Y doped oxides (see **Fig. SI 4**) supporting the active role of Ni^{2+} in promoting the creation of oxygen vacancies in the catalysts.

On the basis of H_2 consumption of the α peak, considering that 1 mmol of H_2 is supposed to react with 1 mmol of O^{2-} species per oxygen vacancy, the V_0 content (%) was calculated on the basis of the Eq. (2) (see experimental part) and is given in **Table 1**.

The broad reduction peak in the range ~230-450 °C, herein called β, that can be divided into 2 different features i.e. β_1 and β_2 was assigned to the reduction of NiO species with different metal-support interaction.[30,53,63] The β_1 peak can be attributed to the

reduction of bulk NiO that has weak interaction with the support or to un-interacted NiO crystallites,[30,64] while the β_2 peak corresponds to NiO nanoparticles more interacting with the support.[33] The β_1 and β_2 peaks shift towards higher temperature at higher Y loading, from 0.5 to 2 wt.%, confirming strong metal-support interaction with the best synergy achieved at 2 wt.% Y. Moreover, at high Y loading the two features β_1 and β_2 become less defined overlapping into a single broad peak, suggesting that such peak contains the contribution from several species that are reduced simultaneously. According with the literature and as results from **Fig. SI 4** and **Table SI 6**,[30,33,60] the reduction of ceria surface occurs with maximum at ~490-505 °C. Therefore, the β peak may correspond to the concomitant reduction of nickel species and ceria surface and the broader is the peak, such as that detected for 5Ni/CeO_2-Y2.0%,the higher the intimate contact is.

The high temperature, (T > 800 °C), the peak, labeled γ in **Fig. 1** (and **Fig. SI 4**) corresponds to the bulk reduction of the CeO_2-based oxides.[60,65]

According to the H_2 consumption values reported in **Table 1** and considering that the theoretical amount required for the overall reduction of NiO to metallic Ni is 0.85 mmol/g_{cat}, on the basis of a real Ni loading equal to 5 wt%, the β reduction peak (ranging between 1.17-1.20mmol/g_{cat}) contains the contribution from NiO along with surface ceria reduction. Similar H_2 consumptions of the β peak were registered for Ni/CeO_2 and Ni/CeO_2-Y catalysts confirming that the catalysts contain, overall, comparable amount of NiO/Ni^{2+} species. As it concerns the γ peak, the H_2 consumption decreases as the increase of Y content (0-5 wt.%), in accord with higher oxygen vacancies in the catalysts.[30,34] Such trend was confirmed by XPS analysis (**Table SI5**) and by TPR of selected supports. From values listed in **Table SI 6**, it results that moving from CeO_2 to CeO_2-Y0.5% and to

CeO_2-Y 2.0% the hydrogen consumption of the β peak gradually increased, especially for Y 2.0%, according with higher SSA (**Table SI2**). Conversely, the hydrogen consumption of the γ peak decreased and, in the whole, the β + γ uptake decreased in line with an increased oxygen vacancy concentration.

For $5Ni/Y_2O_3$, only a broad peak between ~300-500 °C was registered with two maxima at 330 and 435 °C and according to the previous notation we will continue to label such peaks as β_1 and β_2. For comparison, the TPR of the Y_2O_3 support was registered showing a peak centred at ~ 550 °C with H_2 consumption of 0.31 mmol/g_{cat} (see **Fig. SI 4** and **Table SI 6**). The total H_2 consumption for $5Ni/Y_2O_3$ is 1.29 mmol/g_{cat}, which exceeds the theoretical value required for the total reduction of NiO to metallic Ni (0.85 mmol/g_{cat}) and, as well, 1.16 mmol/g_{cat} (corresponding to the sum 0.85 plus 0.31mmol/g_{cat}, that is the H_2 consumption of the yttria oxide), suggesting that new oxygen vacancies are created in the Y_2O_3 after Ni deposition.

Bellido et al.[66] studied the effect of Y_2O_3-ZrO_2 composition on Ni/Y_2O_3-ZrO_2 catalysts and they found that the reduction of pure Y_2O_3 support only accounted for a small fraction of the hydrogen consumption in the H_2-TPR. However, the reduction behavior of the Ni/Y_2O_3-ZrO_2 supports was significantly influenced by the interaction among the species and the introduction of Y^{3+} into ZrO_2 as well as likely of Ni^{2+}creates new oxygen vacancies to preserve overall electroneutrality. According to the literature and based on our experimental results,[67] the H_2 consumption values registered for $5Ni/Y_2O_3$ and Y_2O_3 were attributed to the reduction of NiO and as well to the reduction of oxygen species chemisorbed on the yttria support.

Table 1. Reduction temperatures at the peak maximum (T_{max}) and H_2 consumption values of the calcined catalysts derived from H_2-TPR.

Catalyst	T_{max} (ºC)				H_2 consumption (mmol/g_{cat})			V_0 (%)[a]
	α	β_1	β_2	γ	α	$\beta(\beta_1+\beta_2)$	γ	
5Ni/CeO_2	207	283	379	873	0.26	1.17	0.73	2.36
5Ni/CeO_2- Y0.5%	209	286	381	871	0.29	1.20	0.67	2.62
5Ni/CeO_2- Y1.0%	209	286	381	871	0.30	1.20	0.62	2.70
5Ni/CeO_2- Y2.0%	240	316	385	872	0.44	1.21	0.59	3.95
5Ni/CeO_2- Y5.0%	225	294	390	873	0.33	1.20	0.59	2.92
5Ni/Y_2O_3	-	330	435	-	-	1.29	-	

[a]Oxygen vacancies (%) calculated from α peak

3.1.3 Morphologies of the catalysts derived from TEM and HRTEM characterization

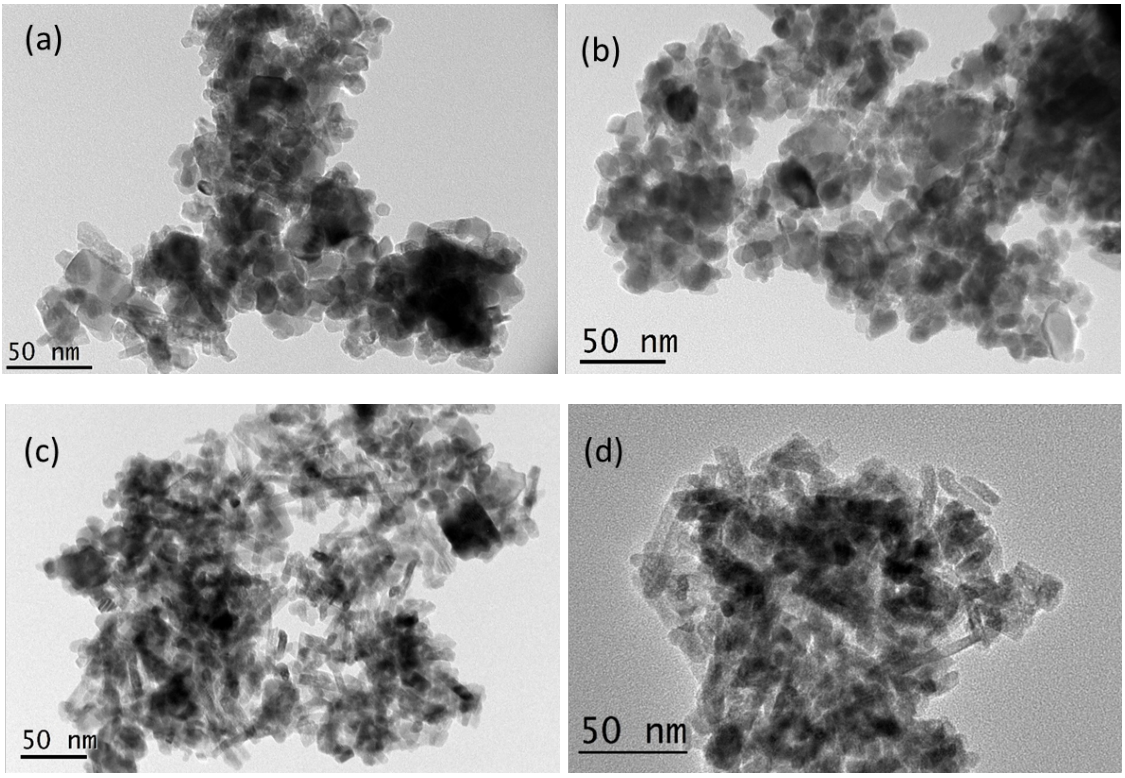

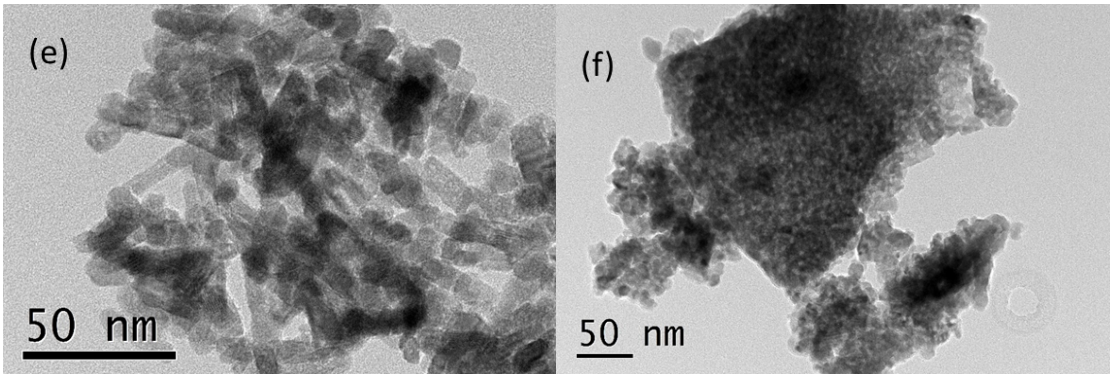

Fig. 4.1.TEM micrographs of the catalysts reduced at 550 °C for 1h in 5% H_2/Ar (100 mL/min); (a) 5Ni/CeO_2, (b) 5Ni/CeO_2-Y0.5%, (c) 5Ni/CeO_2-Y1.0%, (d) 5Ni/CeO_2-Y2.0%, (e) 5Ni/CeO_2-Y5.0%, (f) 5Ni/Y_2O_3.

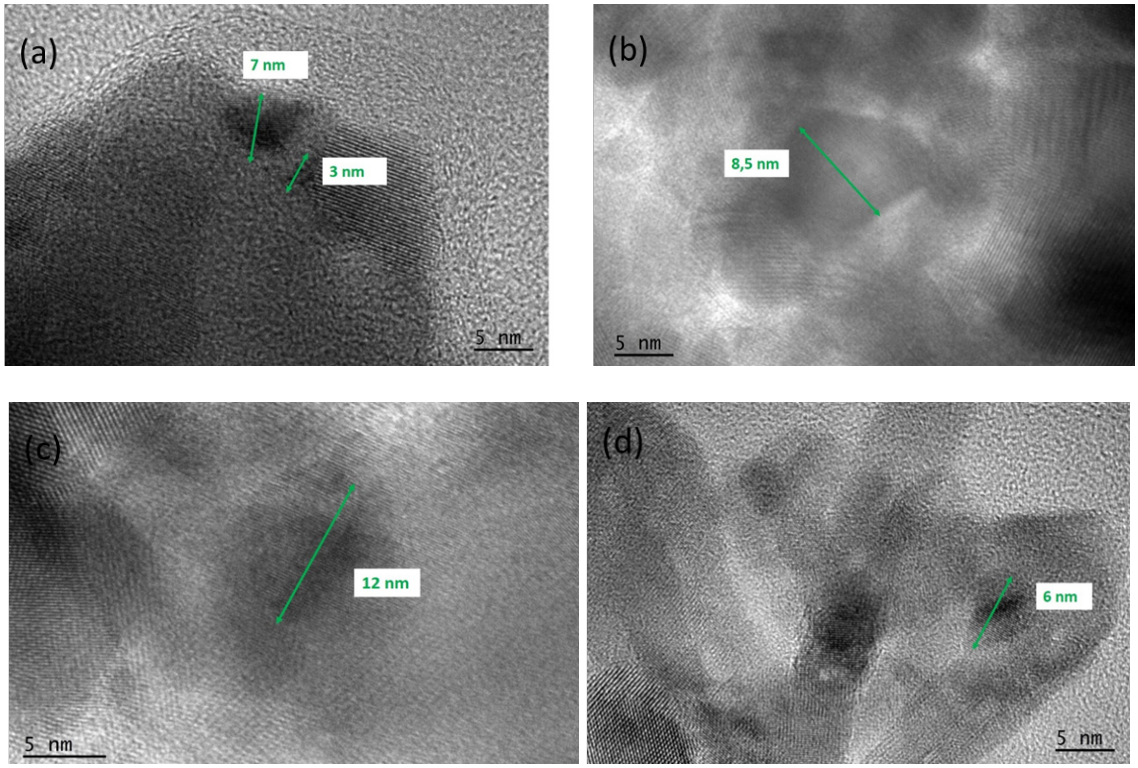

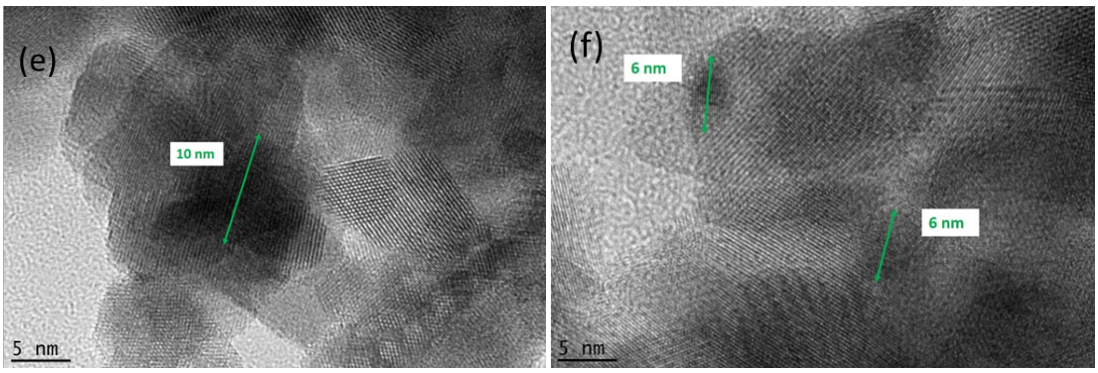

Fig. 4.2. HRTEM micrographs of the catalysts; Condition: reduced at 550 °C for 1h in 5% H_2/Ar (100 mL/min); (a) 5Ni/CeO_2, (b) 5Ni/CeO_2-Y0.5%, (c) 5Ni/CeO_2-Y1.0%, (d) 5Ni/CeO_2-Y2.0%, (e) 5Ni/CeO_2-Y5.0%, (f) 5Ni/Y_2O_3.

In order to gain more morphology information of the catalysts, the high-resolution transmission electron microscopy (HRTEM) and TEM analyses were conducted over the reduced samples using the same reduction condition as activity test. The micrographs of reduced catalysts were shown in **Fig. 4.1 (a-f) and 4.2 (a-f).**

It can be clearly seen from **Fig. 4.1** that all the catalysts contain well-defined crystallites and that the introduction of Y tailors the particle sizes of CeO_2 in the catalysts. In the absence of Y as shown in **Fig. 4.1a**, CeO_2 was constituted by nanoparticles (NPs) as irregular polyhedrals with some aggregated particles exceeding 50 nm. In **Fig. 4.1b**, the CeO_2 particles promoted with 0.5 wt.% of Y became smaller than for pure ceria. For higher concentrations of Y, nanorods (NRs) appeared (**Fig.4.1c-e)**. It was difficult to evaluate the proportion of nanorods, but we noted that on one side the NPs size decreased and on the other the NRs became thinner. The influence of Y concentration on average grain size and the morphology is summarized in **Table SI 7** where the measurements obtained from the TEM images are listed. The formation of nanorods with high exposed surface area detected from 1 to 2 wt.% of Y complies with the increased intensity of the α

peak, attributed to the reduction of oxygen species chemisorbed on oxygen vacancies, and is in line with the highest SSA of the Ni/CeO_2-Y2%. The aspects of the NRs are presented in **Fig. SI 5**. We see clearly the decrease in size of nanorods from 1wt.% Y (**Fig. SI 5a)** to 5 wt.% Y (**Fig. SI 5c)**. All catalysts are well crystallized as evidenced by the lattice planes. The nanorod of 5Ni/CeO_2-Y2% **(Fig. SI 5d)** reveals the (111) and (220) planes corresponding to the distance of 3.12 and 1.91 Å, respectively. The NPs as for them showed frequently the (111) facets. Therefore, Y addition does not produce significant modification into the CeO_2 lattice in agreement with XRD characterization.

For the pure Ni/Y_2O_3 sample, large aggregate nanoparticles of 10-15 nm were detected, see **Fig. 4.1f**.

From the data so far reported it can be concluded that the morphology of the reduced catalysts changed with the incorporation of Y. The particle size of CeO_2 decreased as increasing Y loading with the formation of nanorods and such trend is in accord with the increase of SSA shown in **Table SI3**. As previously reported in the literature, CeO_2 morphology can be modulated depending on the preparation conditions and nanorods formation is favored during the hydrothermal process.[37]

By simple TEM analysis, the size distribution of Ni^0 nanoparticles cannot be distinguished according to another author's report.[37] In order to obtain more detailed information on nickel particle sizes, HRTEM images and EDX spectra were recorded and are shown in **Fig.4.2 and Fig. SI 6, respectively**, where the measured sizes of Ni^0 nanoparticles are marked, mapping was also carried out.

HRTEM images show that the Ni metallic particles are spherical and well dispersed on the support. The average size was ranging from 6-12 nm for all catalysts. The Ni

metallic particles were detected by the lattice planes of 2.03 or 1.76 Å corresponding respectively to the (111) or (002) planes of the fcc structure of nickel.

The EDX spectra show that the signals of Ni and Ce keep stable with the increase of Y loading, indicating again high dispersion of Ni. For the 5Ni/CeO_2-Y2.0% sample the composition homogeneity of Ni and Y was confirmed by Scanning TEM-Energy Dispersive X-ray Spectroscopy (STEM-EDX) mapping (**Fig. SI 7**).

In the overall, Ni^0 resulted well dispersed on all CeO_2-based catalysts as confirmed by XRD results. Moreover, Y doping promotes the decrease of the CeO_2 particle size and the formation of CeO_2 nanorods.

3.1.4. Evaluation of oxygen vacancies content and oxygen mobility by TGA analysis

In order to evaluate the surface oxygen vacancies content and the oxygen mobility of the Ni/CeO_2 supported (Y-modified and Y-free) catalysts, temperature-programmed desorption curves of adsorbed oxygen (O_2-TPD) were registered over the reduced catalysts by performing thermal gravimetric analyses (TGA). The acquired TGA profiles are displayed in **Fig. SI8**. It can be seen from the figure that the reduced catalysts, after saturation with pure O_2, undergo distinct weight losses under N_2 atmosphere from room temperature until 600 °C as the desorption of adsorbed oxygen occurs. For simplicity, the curves were divided into three parts according to the weight loss slope in the different range of temperatures, i.e. sharp, fast and stable loss. So, the weight loss at the temperature below about 150 °C was ascribed to the removal of weakly adsorbed oxygen (physisorbed O_2), between ~150-400°C desorption of chemisorbed O_2 takes place, while in the range 400-600 °C or even above 600 °C the removal of bulk oxygen species should occur. In our case, a stable trend was observed up to 600 °C according to the TPR curves

since ceria bulk reduction occurred above 800 °C.

At low temperature and in the range 150-400 °C, the weight loss intensity increased as a function of Y loading, from Ni/CeO_2 Y-free until 2 wt.%, then, for Y of 5 wt.% a decrease was observed, being the TGA curve of such sample intermediate between Y 2 wt.% and Y1 wt.%. Looking in details at the profile of 5Ni/CeO_2-Y2.0%, the sharp weight loss occurring from room temperature up to ~110 °C corresponds to -0.82%, while by increasing the temperature up to 400 °C, an overall weight loss of -1.53%was registered. Assuming that the so far discussed weight losses correspond to O_2 released from the sample, therefore, the mmol of oxygen removed were calculated: below 150 °C 0.25 mmol O_2/g_{cat} (physisorbed oxygen) and in the overall 0.47 mmol O_2/g_{cat} up to 400 °C are desorbed. Therefore, the amount of chemisorbed O_2 is equal to 0.22 mmol/g_{cat}. Such value is the half amount of the H_2 consumption value registered for the α peak in the TPR experiment (see **Table 1**). Considering that 1 mmol of H_2 reacts with 1 mmol of O^{2-} species per oxygen vacancy, such finding is in agreement with the assumption that the α peak is due to the reduction of oxygen species adsorbed on the vacancies.

In conclusion, TGA analyses confirmed that Y dopant promoted the formation of oxygen vacancies in our samples, the highest content being achieved for Y 2 wt.%, according with other characterizations in this study and literature results.[43,44,62,63]

3.1.5 Basicity distribution of the reduced catalysts derived from CO_2-TPD analyses

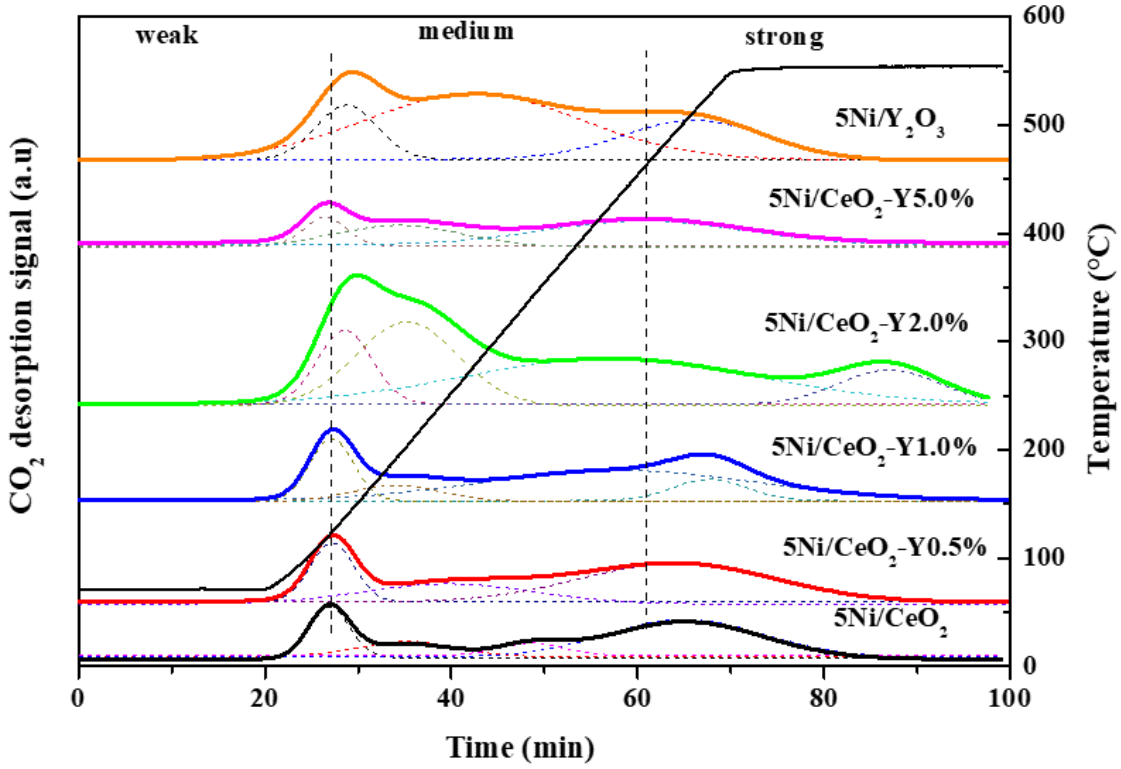

Fig. 5. CO_2-TPD profiles registered over reduced catalysts; Pretreatment condition: Reduction at 550 ˚C for 1 h in 5% H_2/Ar (50 mL/min), cooling down to 80 ˚C and He purging, then CO_2 adsorption under 10% CO_2/Ar for 1 h (50 mL/min).

In order to investigate the basicity of the reduced catalysts, CO_2-TPD experiments were performed on above catalysts. The CO_2-TPD profiles are plotted in **Fig. 5,** the concentration and distribution of basic sites are listed in **Table 2**. As shown in **Fig. 5**, the CO_2 desorption curves can be divided into three regions according to the temperatures, i.e. T <150 ˚C, between 200-450 ˚C and T >450 ˚C, corresponding to the weak, medium and strong basic sites, respectively.[68] It is shown that the distribution of basic sites changed significantly with the increase of yttrium loading, in particular, the CO_2 desorption peaks of Y-modified catalysts shifted towards higher temperature as the increase of Y until 2

wt.%. Moreover, as reported in **Table 2**, the concentration of weak and medium + strong basic sites (as overall amount) increase as the increase of Y (up to 2.0 wt%), with slight decreased values for Y 5.0%. The highest basicity was registered for the 5Ni/CeO_2-Y2.0% sample, while Ni/Y_2O_3 was in between Y 1.0 wt% and Y 5.0 wt%.

Table 2. Basic sites distribution calculated from CO_2-TPD for Y-promoted catalysts after reduction at 550°C

Catalyst	Basic sites [μmol/g_{cat}]				Distribution of basic sites [%]		
	Weak	Medium	Strong	Total basicity	Weak	Medium	Strong
5Ni/CeO_2	18.2	13.3	63	95	19.2	14.1	66.7
5Ni/CeO_2- Y0.5%	22.1	8.8	87.4	118	18.7	7.5	73.8
5Ni/CeO_2- Y1.0%	25.1	23.7	76.7	126	20.0	18.9	61.1
5Ni/CeO_2- Y2.0%	35.4	75.5	140.7	251	14.1	30.0	55.9
5Ni/CeO_2- Y5.0%	32.3	71.3	129.0	233	13.9	30.6	55.5
5Ni/Y_2O_3	30.9	55.9	77.8	165	18.8	34.0	47.2

3.2 Catalytic performance of different catalysts in CO_2 methanation

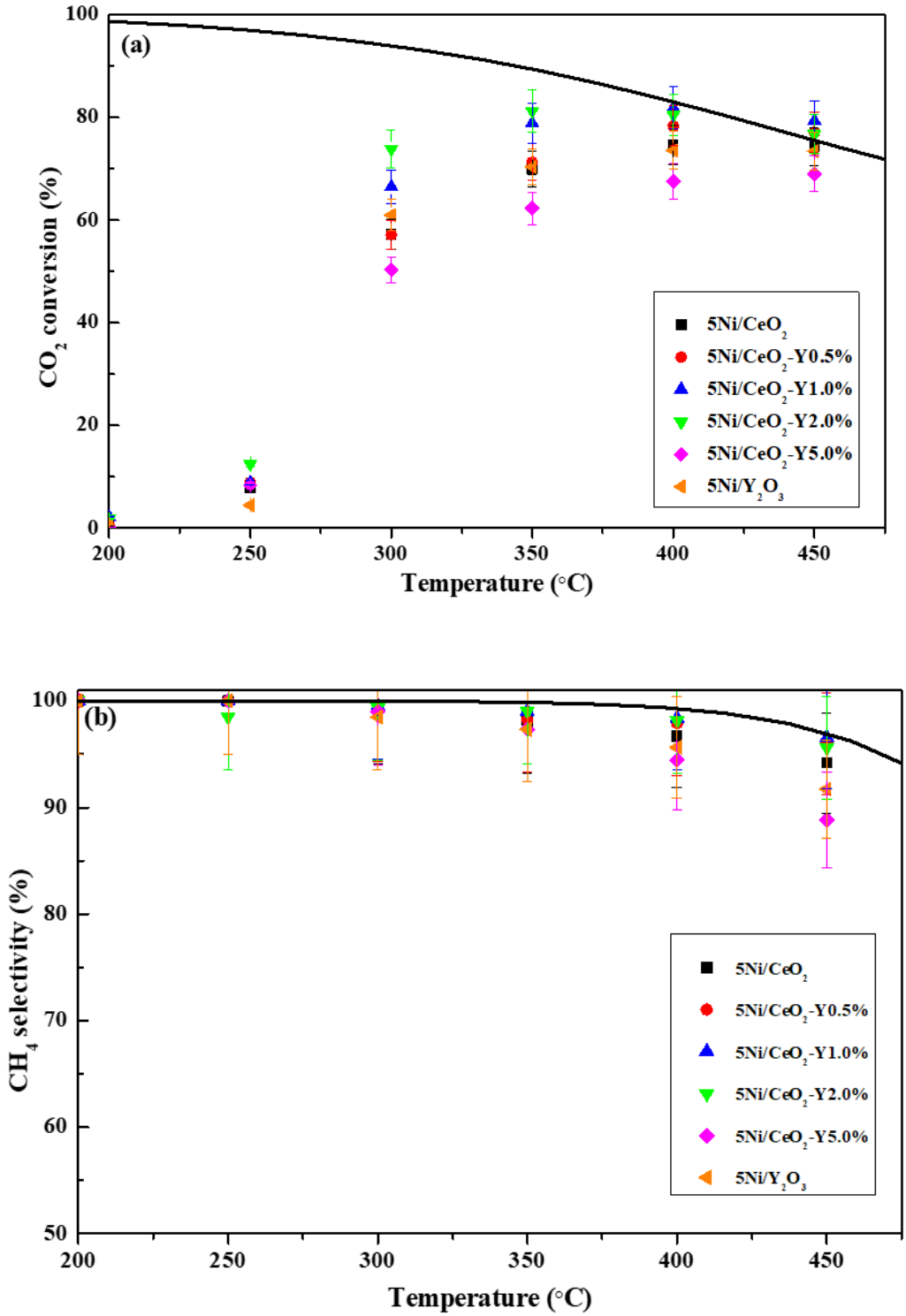

Fig. 6. Catalytic performances in methanation reaction as function of the temperature over the catalysts; (a) CO_2 conversion (b) CH_4 selectivity; Reaction conditions: WHSV=60,000 $h^{-1}gcat^{-1}$; $CO_2/H_2/Ar$=15/60/25; atmospheric pressure.

The catalytic performance in CO_2 methanation were investigated over the Ni catalysts supported over Y-modified CeO_2, pure CeO_2 and pure Y_2O_3 and the CO_2 conversion and CH_4 selectivity values are displayed in **Fig. 6** along with the thermodynamic curves given for comparison. These results are in line with those presented in the literature in similar experimental conditions (**Table SI 8**). As shown in **Fig. 6a**, the highest CO_2 conversions for all the catalysts were obtained at 400 °C, which were close to the theoretic value, except for the sample of 5Ni/CeO_2-Y5.0%, which reached the highest conversion at 450 °C. In the temperature range of 250-350 °C, the CO_2 conversion for Y-modified catalysts gradually increased as the increase of yttrium up to 2 wt.% Y, afterwards, the activity declined sharply when yttrium content reached 5 wt.%, which was less active than the 5Ni/Y_2O_3 catalyst. The 2 wt.% Y modified catalyst possessed the highest CO_2 conversion compared to the other catalysts at 250-350 °C. From **Fig. 6b,** it can be found that the CH_4 selectivity of all catalysts at low temperature (200-250 °C) appears very close to that of the theoretical value. Afterwards, by further increase the temperatures up to 300-450 °C, the selectivity of all catalysts decreases gradually, and the worst value was obtained for 5Ni/CeO_2-Y5.0% and 5Ni/Y_2O_3 at temperature higher than 400 °C.

In brief, the doping of yttrium into CeO_2 has a significant effect on the activity and selectivity of the Ni catalysts towards the Sabatier's reaction. The Ni catalyst supported over CeO_2 modified by 2 wt.% Y possesses the best CO_2 conversion and high CH_4selectivity at relatively low temperature (i.e. 300-350 °C).

3.3 Relationships between physico-chemical properties and catalytic performances

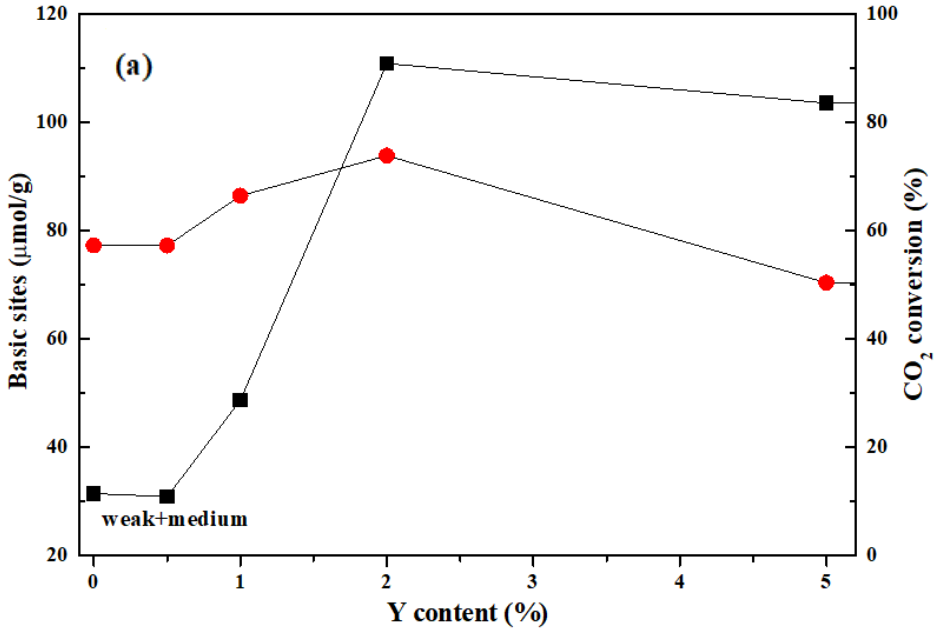

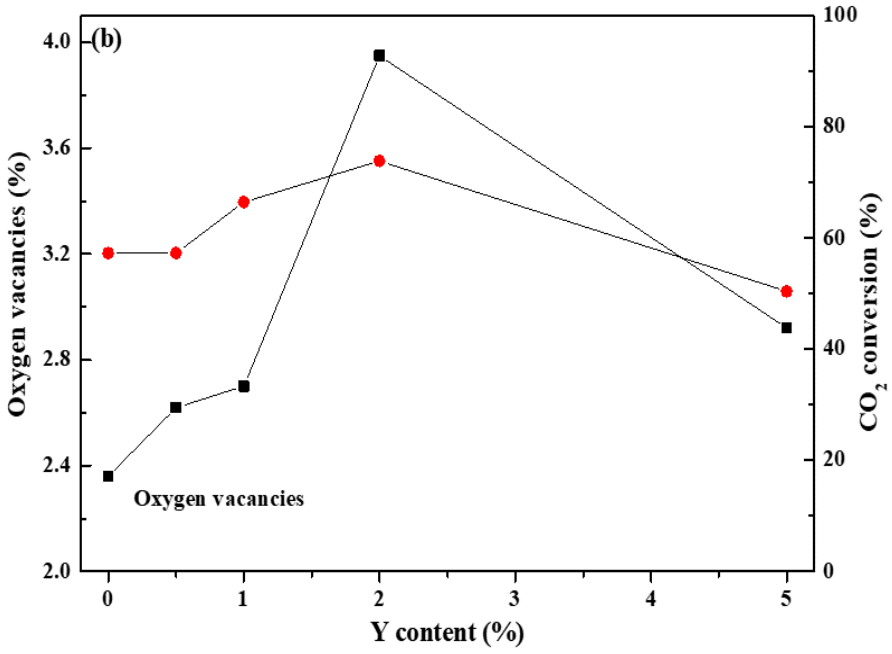

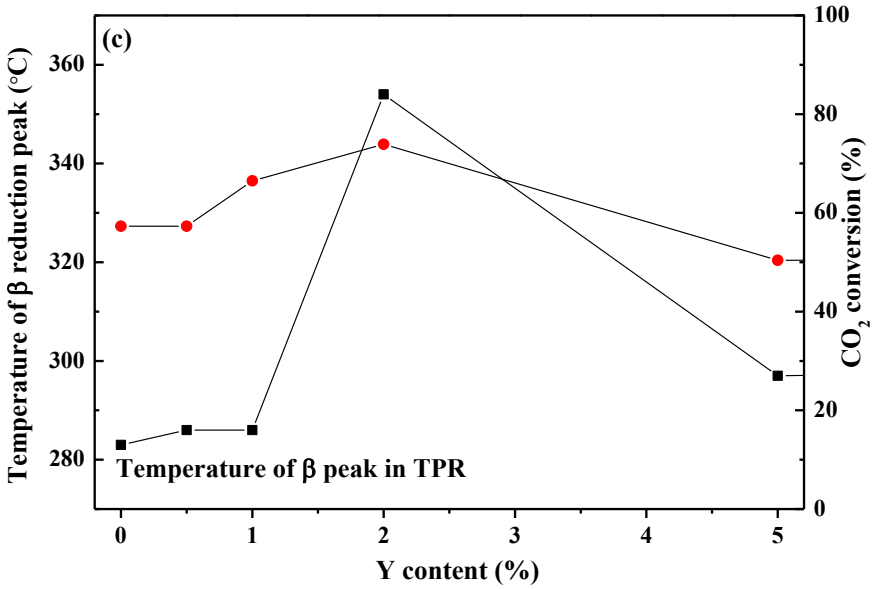

Fig. 7. Correlation of CO_2 conversion (at 300 °C) with (a) basic sites; (b) oxygen vacancies content, V_0 (%); (c) temperature of β reduction peak in the TPR. The Y content represents the loading of Y for Ni/CeO_2-Y catalysts, with 0% representing 5Ni/CeO_2.

The mechanism of CO_2methanation over Ni/CeO_2 catalysts has been studied in the literature.[35,69,70] It was attributed to the synergistic effect of two types of active sites, i.e. the active sites at the Ni-Ce-O interface for CO_2 adsorption and dissociation as well as the Ni^0 sites for H_2 adsorption and dissociation. The H_2 dissociated to H- species on the surface of metallic nickel, and the CO_2 adsorbed on the surface of support and then dissociated to carbonate or hydrogen carbonate species, then the carbonate or hydrogen carbonate were hydrogenated to formate species including monodentate and bidentate formate. The monodentate formate could be hydrogenated to methane faster than bidentate formate specie. The larger is the metallic nickel surface area formed on the catalyst by small Ni particles, the more favorable the adsorption and dissociation of H_2 are.

As shown in **Fig. 7 (a, b and c),** good relations were found at increasing Y loading

between CO_2 conversion at 300 °C and the number of basic sites (weak + medium) ($\mu mol/g_{cat}$) (**Fig. 7 a**) as well as between CO_2 conversion at 300 °C and the oxygen vacancies content, V_0 (%) (see **Table 1**) (**Fig. 7b**). A similar trend, at increasing Y loading, was observed between CO_2 conversion at 300 °C and the temperatures of β reduction peak that is related to the strength of the metal-support interaction of Ni over CeO_2-Y catalysts.

The CO_2 conversion at 300 °C was chosen for comparison because at low temperature (<300 °C) the results of CO_2 conversion were not very distinguishing. Meanwhile, the CO_2 conversion of all catalysts increases with the increase of temperature (350-450 °C, **Fig. 7**), which also makes the difference of catalytic performance unnoticeable. Thus, the 300 °C can be an appropriate temperature for comparison.

So, on the basis of the so far reported data and in agreement with the methanation reaction mechanism previously mentioned,[35] it can be concluded that the decrease of CeO_2 particles, the high dispersion of nickel as well as the formation of more oxygen vacancies provide more active sites for the adsorption and dissociation of hydrogen and CO_2. Moreover, the high metal-support interaction depresses the sintering of active metal. For 5Ni/CeO_2-Y2.0% sample, highly dispersed nickel particles provide more active sites for the adsorption and dissociation of hydrogen, the highest number of oxygen vacancies favors the adsorption of CO_2 and the highest amount of medium basic sites promotes the formation of monodentate formate, which can be fast hydrogenated to methane. Thus, the highest CO_2 conversion and relatively high CH_4 selectivity were obtained on the catalyst.

3.4 Steady-state test of Ni/CeO_2 based catalysts in CO_2 methanation

In order to evaluate the stabilities in CO_2 conversion and CH_4 selectivity, 5Ni/CeO_2-Y1.0% and 5Ni/CeO_2-Y2.0% were selected for steady state tests at 300 °C for 7 h. The temperature of 300 °C was selected due to the recognizable difference of CO_2 conversion values shown in **Fig. 6**. The 5Ni/CeO_2 sample was used for comparison. The selected catalysts were reduced in the same condition as for CO_2 methanation test, then were cooled down to 300 °C and the reaction gas mixture was fed into the reactor. The steady state test results are displayed in **Fig. SI9**. It can be seen from **Fig. SI9a** that the CO_2 conversion values of all samples decrease slightly at the beginning, then keep stable on stream. Both Y promoted catalysts performed better than Ni/CeO_2, with 5Ni/CeO_2-Y2.0% showing the best CO_2 conversion. The results of 5Ni/CeO_2 were slightly higher than those shown in **Fig. 6a**. This was attributed to possible effects, within the experimental error of 5%, during the catalytic tests. The selectivity to CH_4 is shown in **Fig. SI9b**, the values maintain nearly stable during the test and both Y-modified catalysts achieved higher selectivity than Ni/CeO_2 catalyst.

The slight difference in the conversions (lower than 3%) between catalytic tests from 200 °C to 450 °C and steady-state experiments can be explained by the fact that, in the former case, the catalysts were exposed to a lower temperature (250°C) for at least 30 min, as described in experimental part, prior to reach 300°C.

3.5 Characterization of Ni/CeO_2 based catalysts after steady state test

3.5.1 XRD patterns of the catalysts after steady state test

In order to investigate structural modifications of the catalysts after steady state test, XRD patterns were registered and are shown in **Fig. SI10**. No diffraction peaks of

metallic nickel or NiO were found, meaning that the nickel species remained highly dispersed on the support even after steady state test at 300 °C for 7h, confirming the XRD results of the catalysts after activity test. A perusal of **Fig. SI10b** (enlarged pattern in the range between 42-52 ° 2θ) shows a slight shift to higher angles of all CeO_2 and CeO_2-Y peaks in comparison with **Fig. 2a**, especially in the case of 5Ni/CeO_2-Y2.0% which (202) peak is centered at 47.65 °2θ. This finding would point to a further inward diffusion of Y^{3+} and Ni^{2+} into the ceria lattice, as suggested by XPS analysis (see **Table SI10**).

In **Table SI9** the particle sizes of CeO_2 support calculated by Debye-Scherrer equation are listed. The values are close with those given in **Table SI4**, showing that no sintering of ceria nanoclusters takes place at 300 °C under reaction stream. The 5Ni/CeO_2-Y2.0% maintained the smallest particle size of ceria. Such results account for the good stability in CO_2 conversion and CH_4 selectivity registered being the sintering of active metals the main reason of deactivation in Sabatier's reaction.[34]

3.5.2 XPS analysis of the catalysts after steady state test

In order to obtain the surface composition and oxidation states of the catalysts after steady test, the XPS analyses of the spent catalysts were performed. The Ce3d XPS spectra of the samples are displayed in **Fig. SI11,** while the Ni2p and the O1s regions are reported in **Fig. SI 12** and **Fig. SI 13**, respectively. **Table SI10** reports the surface oxidation state, atomic ratio and binding energies of samples after steady state. As already shown in **Fig. SI3**, the Ce3d spectra were fitted with 10 peaks, in which four peaks are attributed to Ce (III) and six peaks are attributed to Ce (IV). Because of the small

dimension of the nickel particles, surface reoxidation occurs after catalytic reaction, likely during exposure to the atmosphere, so it was impossible to calculate the degree of nickel reduction. Compared to the XPS results of calcined samples (**Table SI5**), a small decrease of the Ni/Ce ratio was found (**Table SI10**). Conversely, the Y/Ce ratio decreased by an important extent, indicating a probable inward diffusion of yttrium into the bulk, according with XRD results (see **Fig. SI10b**). The Ce (III) % of the samples nearly keep the same value as those of calcined samples, meaning that the surface Ce^{3+} species of the catalysts were oxidized after exposure to the atmosphere, while the values (%) of OOH decreased a little in comparison with those of the calcined samples. Considering that the OOH surface concentration may be influenced by the atmosphere, the decrease of these percentage may be a consequence of the exposition to the reaction mixture. A decrease of the Ni/Ce ratio and a simultaneous shift of Ni2p3/2 peak at higher energies suggest a small increases of Ni particles size after the steady state test and a different interaction with the support.

As previously stated for calcined samples, there is no significant difference regarding to binding energy of $Y3d_{5/2}$.

4. Conclusions

Y-modified CeO_2 nanoparticles have been successfully synthesized by hydrothermal method and used as supports for Ni deposition by wetness impregnation. The catalytic performances of Ni/CeO_2 nanoparticles with/without Y were investigated in CO_2 methanation reaction and are discussed in line with physico-chemical characterizations of calcined, reduced and spent catalysts. This article represents the first

investigation on the effect of yttrium on Ni/CeO_2 catalysts for CO_2 methanation.

The specific surface area of Ni/CeO_2-Y samples, the crystallite sizes of ceria, the oxygen vacancies content and the interaction between NiO and CeO_2 can be tuned by different Y content as shown by N_2 adsorption/desorption, XRD, XPS, TPR, HRTEM, TGA, CO_2-TPD. All the catalysts contain well-defined crystallites and the introduction of Y tailors the particle sizes and shapes of CeO_2 nanoparticles in the catalysts. Unpromoted CeO_2 particles are nanoparticles turning to a mix of nanoparticles and nanorods by Y promotion, with an increase of the nanorods size of up to 2 wt.% of Y addition.

Highly dispersed Ni active sites in strong interaction with the ceria-based oxide and the oxygen vacancies formed by Y addition are the key factors determining high catalytic activity and stable performances of the Ni/CeO_2-Y catalysts between 250-350 °C with high selectivity towards methane formation.

The Ni/CeO_2-Y 2.0% with the highest number of oxygen vacancies able to activate CO_2 and with the strongest metal-support interaction suppressing sintering of the Ni sites for H_2 activation, was the best performing CO_2 methanation catalyst.

Author Contributions

The manuscript was written through contributions of all authors. All authors have given approval to the final version of the manuscript.

Acknowledgments

Leonarda F. Liotta carried the research in the field of the COST Action 18224 “Green

Chemical Engineering Network towards upscaling sustainable processes" and acknowledges the CNR Program Short Term Mobility (2018) for supporting her research mobility in Sorbonne Université. The Italian project PON MIUR "Energy for TARANTO" (Proposal Code ARS01_00637) is also acknowledged for supporting the research activity at the ISMN-CNR.

The authors are grateful to Nunzio Gallì (ISMN-CNR) for carrying out specific surface area and porosity measurements. Chao Sun acknowledges the China Scholarship Council (CSC) for the financial support in his PhD research in Sorbonne Université.

References

(1) Peter, S. C. Reduction of CO2 to Chemicals and Fuels: A Solution to Global Warming and Energy Crisis. *ACS Energy Lett.* **2018**, *3* (7), 1557–1561. https://doi.org/10.1021/acsenergylett.8b00878.

(2) Younas, M.; Loong Kong, L.; Bashir, M. J. K.; Nadeem, H.; Shehzad, A.; Sethupathi, S. Recent Advancements, Fundamental Challenges, and Opportunities in Catalytic Methanation of CO2. *Energy and Fuels* **2016**, *30* (11), 8815–8831. https://doi.org/10.1021/acs.energyfuels.6b01723.

(3) Aziz, M. A. A.; Jalil, A. A.; Triwahyono, S.; Ahmad, A. CO2 Methanation over Heterogeneous Catalysts: Recent Progress and Future Prospects. *Green Chem.* **2015**, *17* (5), 2647–2663. https://doi.org/10.1039/c5gc00119f.

(4) Füssel, H. M. An Updated Assessment of the Risks from Climate Change Based on Research Published since the IPCC Fourth Assessment Report. *Clim. Change* **2009**, *97* (3), 469–482. https://doi.org/10.1007/s10584-009-9648-5.

(5) Peters, M.; Köhler, B.; Kuckshinrichs, W.; Leitner, W.; Markewitz, P.; Müller, T. E. Chemical Technologies for Exploiting and Recycling Carbon Dioxide into the Value Chain. *ChemSusChem* **2011**, *4* (9), 1216–1240. https://doi.org/10.1002/cssc.201000447.

(6) Yan, Y.; Dai, Y.; Yang, Y.; Lapkin, A. A. Improved Stability of Y2O3 Supported Ni Catalysts for CO2 Methanation by Precursor-Determined Metal-Support Interaction. *Appl. Catal. B Environ.* **2018**, *237* (June), 504–512. https://doi.org/10.1016/j.apcatb.2018.06.021.

(7) Ghaib, K.; Ben-Fares, F. Z. Power-to-Methane: A State-of-the-Art Review. *Renew. Sustain. Energy Rev.* **2018**, *81* (June 2017), 433–446. https://doi.org/10.1016/j.rser.2017.08.004.

(8) Park, J. N.; McFarland, E. W. A Highly Dispersed Pd-Mg/SiO2 Catalyst Active for Methanation of CO2. *J. Catal.* **2009**, *266* (1), 92–97. https://doi.org/10.1016/j.jcat.2009.05.018.

(9) Prairie, M. R.; Renken, A.; Highfield, J. G.; Ravindranathan Thampi, K.; Grätzel, M. A Fourier Transform Infrared Spectroscopic Study of CO2 Methanation on Supported Ruthenium. *J. Catal.* **1991**, *129*, 130–144. https://doi.org/10.1016/0021-9517(91)90017-X.

(10) Solymosi, F.; Erdöhelyi, A. Methanation of CO2 on Supported Rhodium Catalysts. *J. Catal.* **1981**, *68*, 371–382.

(11) Weatherbee, G. D.; Bartholomew, C. H. Hydrogenation of CO2 on Group VIII Metals. IV. Specific Activities and Selectivities of Silica-Supported Co, Fe, and Ru. *J. Catal.* **1984**, *87* (2), 352–362. https://doi.org/10.1016/0021-9517(84)90196-9.

(12) Shin, H. H.; Lu, L.; Yang, Z.; Kiely, C. J.; McIntosh, S. Cobalt Catalysts Decorated with Platinum Atoms Supported on Barium Zirconate Provide Enhanced Activity and Selectivity for CO2 Methanation. *ACS Catal.* **2016**, *6* (5), 2811–2818. https://doi.org/10.1021/acscatal.6b00005.

(13) Le, T. A.; Kim, M. S.; Lee, S. H.; Kim, T. W.; Park, E. D. CO and CO2 Methanation over Supported Ni Catalysts. *Catal. Today* **2017**, *293–294*, 89–96. https://doi.org/10.1016/j.cattod.2016.12.036.

(14) Wierzbicki, D.; Baran, R.; Dębek, R.; Motak, M.; Gálvez, M. E.; Grzybek, T.; Da Costa, P.; Glatzel, P. Examination of the Influence of La Promotion on Ni State in Hydrotalcite-Derived Catalysts under CO2 Methanation Reaction Conditions: Operando X-Ray Absorption and Emission Spectroscopy Investigation. *Appl. Catal. B Environ.* **2018**, *232* (January), 409–419. https://doi.org/10.1016/j.apcatb.2018.03.089.

(15) Wierzbicki, D.; Motak, M.; Grzybek, T.; Gálvez, M. E.; Da Costa, P. The Influence of Lanthanum Incorporation Method on the Performance of Nickel-Containing Hydrotalcite-Derived Catalysts in CO2 Methanation Reaction. *Catal. Today* **2018**, *307* (March 2017), 205–211. https://doi.org/10.1016/j.cattod.2017.04.020.

(16) Wierzbicki, D.; Baran, R.; Dębek, R.; Motak, M.; Grzybek, T.; Gálvez, M. E.; Da Costa, P. The Influence of Nickel Content on the Performance of Hydrotalcite-Derived Catalysts in

CO2 Methanation Reaction. *Int. J. Hydrogen Energy* **2017**, *42*, 23548–23555. https://doi.org/10.1016/j.ijhydene.2017.02.148.

(17) Sharma, S.; Hu, Z.; Zhang, P.; McFarland, E. W.; Metiu, H. CO2 Methanation on Ru-Doped Ceria. *J. Catal.* **2011**, *278* (2), 297–309. https://doi.org/10.1016/j.jcat.2010.12.015.

(18) Guo, M.; Lu, G. The Effect of Impregnation Strategy on Structural Characters and CO 2 Methanation Properties over MgO Modified Ni/SiO2 Catalysts. *Catal. Commun.* **2014**, *54*, 55–60. https://doi.org/10.1016/j.catcom.2014.05.022.

(19) He, S.; Li, C.; Chen, H.; Su, D.; Zhang, B.; Cao, X.; Wang, B.; Wei, M.; Evans, D. G.; Duan, X. A Surface Defect-Promoted Ni Nanocatalyst with Simultaneously Enhanced Activity and Stability. *Chem. Mater.* **2013**, *25* (7), 1040–1046. https://doi.org/10.1021/cm303517z.

(20) Romero-Sáez, M.; Dongil, A. B.; Benito, N.; Espinoza-González, R.; Escalona, N.; Gracia, F. CO2 Methanation over Nickel-ZrO2 Catalyst Supported on Carbon Nanotubes: A Comparison between Two Impregnation Strategies. *Appl. Catal. B Environ.* **2018**, *237* (March), 817–825. https://doi.org/10.1016/j.apcatb.2018.06.045.

(21) Wierzbicki, D.; Debek, R.; Motak, M.; Grzybek, T.; Gálvez, M. E.; Da Costa, P. Novel Ni-La-Hydrotalcite Derived Catalysts for CO2 Methanation. *Catal. Commun.* **2016**, *83*, 5–8. https://doi.org/10.1016/j.catcom.2016.04.021.

(22) Fukuhara, C.; Hayakawa, K.; Suzuki, Y.; Kawasaki, W.; Watanabe, R. A Novel Nickel-Based Structured Catalyst for CO2 Methanation: A Honeycomb-Type Ni/CeO2 Catalyst to Transform Greenhouse Gas into Useful Resources. *Appl. Catal. A Gen.* **2017**, *532*, 12–18. https://doi.org/10.1016/j.apcata.2016.11.036.

(23) Zhou, R.; Rui, N.; Fan, Z.; Liu, C. jun. Effect of the Structure of Ni/TiO2 Catalyst on CO2 Methanation. *Int. J. Hydrogen Energy* **2016**, *41* (47), 22017–22025. https://doi.org/10.1016/j.ijhydene.2016.08.093.

(24) Liu, Q.; Tian, Y. One-Pot Synthesis of NiO/SBA-15 Monolith Catalyst with a Three-

Dimensional Framework for CO2 Methanation. *Int. J. Hydrogen Energy* **2017**, *42* (17), 12295–12300. https://doi.org/10.1016/j.ijhydene.2017.02.070.

(25) Guo, X.; Traitangwong, A.; Hu, M.; Zuo, C.; Meeyoo, V.; Peng, Z.; Li, C. Carbon Dioxide Methanation over Nickel-Based Catalysts Supported on Various Mesoporous Material. *Energy and Fuels* **2018**, *32* (3), 3681–3689. https://doi.org/10.1021/acs.energyfuels.7b03826.

(26) Xu, L.; Wang, F.; Chen, M.; Yang, H.; Nie, D.; Qi, L.; Lian, X. Alkaline-Promoted Ni Based Ordered Mesoporous Catalysts with Enhanced Low-Temperature Catalytic Activity toward CO2 Methanation. *RSC Adv.* **2017**, *7* (30), 18199–18210. https://doi.org/10.1039/c7ra01673e.

(27) Bukhari, S. N.; Chong, C. C.; Teh, L. P.; Vo, D. V. N.; Ainirazali, N.; Triwahyono, S.; Jalil, A. A.; Setiabudi, H. D. Promising Hydrothermal Technique for Efficient CO2 Methanation over Ni/SBA-15. *Int. J. Hydrogen Energy* **2019**, *44* (37), 20792–20804. https://doi.org/10.1016/j.ijhydene.2018.07.018.

(28) Ratchahat, S.; Sudoh, M.; Suzuki, Y.; Kawasaki, W.; Watanabe, R.; Fukuhara, C. Development of a Powerful CO2 Methanation Process Using a Structured Ni/CeO2 Catalyst. *J. CO2 Util.* **2018**, *24* (November 2017), 210–219. https://doi.org/10.1016/j.jcou.2018.01.004.

(29) Singha, R. K.; Shukla, A.; Yadav, A.; Sivakumar Konathala, L. N.; Bal, R. Effect of Metal-Support Interaction on Activity and Stability of Ni-CeO2 Catalyst for Partial Oxidation of Methane. *Appl. Catal. B Environ.* **2017**, *202*, 473–488. https://doi.org/10.1016/j.apcatb.2016.09.060.

(30) Yu, Y.; Chan, Y. M.; Bian, Z.; Song, F.; Wang, J.; Zhong, Q.; Kawi, S. Enhanced Performance and Selectivity of CO2 Methanation over G-C3N4 Assisted Synthesis of Ni-CeO2 Catalyst: Kinetics and DRIFTS Studies. *Int. J. Hydrogen Energy* **2018**, *43* (32), 15191–15204. https://doi.org/10.1016/j.ijhydene.2018.06.090.

(31) Italiano, C.; Llorca, J.; Pino, L.; Ferraro, M.; Antonucci, V.; Vita, A. CO and CO2 Methanation over Ni Catalysts Supported on CeO2, Al2O3 and Y2O3 Oxides. *Appl. Catal. B Environ.* **2020**, *264* (November 2019), 118494. https://doi.org/10.1016/j.apcatb.2019.118494.

(32) Wang, F.; Wei, M.; Evans, D. G.; Duan, X. CeO2-Based Heterogeneous Catalysts toward Catalytic Conversion of CO2. *J. Mater. Chem. A* **2016**, *4* (16), 5773–5783. https://doi.org/10.1039/c5ta10737g.

(33) Tada, S.; Shimizu, T.; Kameyama, H.; Haneda, T.; Kikuchi, R. Ni/CeO2 Catalysts with High CO2 Methanation Activity and High CH4 Selectivity at Low Temperatures. *Int. J. Hydrogen Energy* **2012**, *37* (7), 5527–5531. https://doi.org/10.1016/j.ijhydene.2011.12.122.

(34) Zhou, G.; Liu, H.; Cui, K.; Xie, H.; Jiao, Z.; Zhang, G.; Xiong, K.; Zheng, X. Methanation of Carbon Dioxide over Ni/CeO2 Catalysts: Effects of Support CeO2 Structure. *Int. J. Hydrogen Energy* **2017**, *42* (25), 16108–16117. https://doi.org/10.1016/j.ijhydene.2017.05.154.

(35) Cárdenas-Arenas, A.; Quindimil, A.; Davó-Quiñonero, A.; Bailón-García, E.; Lozano-Castelló, D.; De-La-Torre, U.; Pereda-Ayo, B.; González-Marcos, J. A.; González-Velasco, J. R.; Bueno-López, A. Isotopic and in Situ DRIFTS Study of the CO2 Methanation Mechanism Using Ni/CeO2 and Ni/Al2O3 Catalysts. *Appl. Catal. B Environ.* **2020**, *265*, 118538. https://doi.org/10.1016/j.apcatb.2019.118538.

(36) Ye, R. P.; Li, Q.; Gong, W.; Wang, T.; Razink, J. J.; Lin, L.; Qin, Y. Y.; Zhou, Z.; Adidharma, H.; Tang, J.; Russell, A. G.; Fan, M.; Yao, Y. G. High-Performance of Nanostructured Ni/CeO2 Catalyst on CO2 Methanation. *Appl. Catal. B Environ.* **2019**, *268* (November), 118474. https://doi.org/10.1016/j.apcatb.2019.118474.

(37) Bian, Z.; Chan, Y. M.; Yu, Y.; Kawi, S. Morphology Dependence of Catalytic Properties of Ni/CeO2 for CO2 Methanation: A Kinetic and Mechanism Study. *Catal. Today* **2020**, *347*, 31–38. https://doi.org/10.1016/j.cattod.2018.04.067.

(38) Liu, K.; Xu, X.; Xu, J.; Fang, X.; Liu, L.; Wang, X. The Distributions of Alkaline Earth Metal Oxides and Their Promotional Effects on Ni/CeO2for CO2methanation. *J. CO2 Util.* **2020**, *38*, 113–124. https://doi.org/10.1016/j.jcou.2020.01.016.

(39) Sun, C.; Świrk, K.; Wierzbicki, D.; Motak, M.; Grzybek, T.; Costa, P. Da. On the Effect of Yttrium Promotion on Ni-Layered Double Hydroxides-Derived Catalysts for Hydrogenation of CO2 to Methane. *Int. J. Hydrogen Energy* **2020**. https://doi.org/10.1016/j.ijhydene.2020.03.202.

(40) Taherian, Z.; Shahed Gharahshiran, V.; Khataee, A.; Meshkani, F.; Orooji, Y. Comparative Study of Modified Ni Catalysts over Mesoporous CaO-Al2O3 Support for CO2/Methane Reforming. *Catal. Commun.* **2020**, *145*, 106100. https://doi.org/10.1016/j.catcom.2020.106100.

(41) Świrk, K.; Gálvez, M. E.; Motak, M.; Grzybek, T.; Rønning, M.; Da Costa, P. Dry Reforming of Methane over Zr- and Y-Modified Ni/Mg/Al Double-Layered Hydroxides. *Catal. Commun.* **2018**, *117* (August), 26–32. https://doi.org/10.1016/j.catcom.2018.08.024.

(42) Takano, H.; Kirihata, Y.; Izumiya, K.; Kumagai, N.; Habazaki, H.; Hashimoto, K. Highly Active Ni/Y-Doped ZrO2 Catalysts for CO2 Methanation. *Appl. Surf. Sci.* **2016**, *388*, 653–663. https://doi.org/10.1016/j.apsusc.2015.11.187.

(43) Świrk, K.; Gálvez, M. E.; Motak, M.; Grzybek, T.; Rønning, M.; Da Costa, P. Yttrium Promoted Ni-Based Double-Layered Hydroxides for Dry Methane Reforming. *J. CO2 Util.* **2018**, *27* (August), 247–258. https://doi.org/10.1016/j.jcou.2018.08.004.

(44) Daneshmand-Jahromi, S.; Rahimpour, M. R.; Meshksar, M.; Hafiz, A. Hydrogen Production from Cyclic Chemical Looping Steam Methane Reforming over Yttrium Promoted Ni/SBA-16 Oxygen Carrier. *Catalysts* **2017**, *7* (286), 1–21. https://doi.org/10.3390/catal7100286.

(45) Świrk, K.; Rønning, M.; Motak, M.; Beaunier, P.; Da Costa, P.; Grzybek, T. Ce- and Y-Modified Double-Layered Hydroxides as Catalysts for Dry Reforming of Methane: On the

Effect of Yttrium Promotion. *Catalysts* **2019**, *9* (1), 56. https://doi.org/10.3390/catal9010056.

(46) He, X.; Yang, H. A Novel Strategy to the Synthesis of Na3YSi2O7 from Natural Palygorskite. *Appl. Clay Sci.* **2014**, *101*, 339–344. https://doi.org/10.1016/j.clay.2014.08.025.

(47) Ilieva, L.; Venezia, A. M.; Petrova, P.; Pantaleo, G.; Liotta, L. F.; Zanella, R.; Kaszkur, Z.; Tabakova, T. Effect of Y Modified Ceria Support in Mono and Bimetallic Pd-Au Catalysts for Complete Benzene Oxidation. *Catalysts* **2018**, *8*. https://doi.org/10.3390/catal8070283.

(48) Liu, J.; Zhao, Z.; Wang, J.; Xu, C.; Duan, A.; Jiang, G.; Yang, Q. The Highly Active Catalysts of Nanometric CeO2-Supported Cobalt Oxides for Soot Combustion. *Appl. Catal. B Environ.* **2008**, *84* (1–2), 185–195. https://doi.org/10.1016/j.apcatb.2008.03.017.

(49) Paparazzo, E. Use and Mis-Use of x-Ray Photoemission Spectroscopy Ce3d Spectra of Ce2O3 and CeO2. *J. Phys. Condens. Matter* **2018**, *30* (34). https://doi.org/10.1088/1361-648X/aad248.

(50) Burroughs, P.; Hamnett, A.; Orchard, A. F.; Thornton, G. Satellite Structure in TheX-Ray Photoelectron Spectra of Some Binary and Mixed Oxides of Lanthanum and Cerium. *J. Chem. Soc., Dalt. Trans.* **1976**, 1686–1698.

(51) Preisler, E. J.; Marsh, O. J.; Beach, R. A.; McGill, T. C. Stability of Cerium Oxide on Silicon Studied by X-Ray Photoelectron Spectroscopy. *J. Vac. Sci. Technol. B Microelectron. Nanom. Struct.* **2001**, *19* (4), 1611–1618. https://doi.org/10.1116/1.1387464.

(52) Xu, B.; Zhang, Q.; Yuan, S.; Zhang, M.; Ohno, T. Synthesis and Photocatalytic Performance of Yttrium-Doped CeO2 with a Porous Broom-like Hierarchical Structure. *Appl. Catal. B Environ.* **2016**, *183*, 361–370. https://doi.org/10.1016/j.apcatb.2015.10.021.

(53) Du, X.; Zhang, D.; Shi, L.; Gao, R.; Zhang, J. Morphology Dependence of Catalytic Properties of Ni/CeO2 Nanostructures for Carbon Dioxide Reforming of Methane. *J. Phys.*

Chem. C **2012**, *116* (18), 10009–10016. https://doi.org/10.1021/jp300543r.

(54) Najafpour, M. M.; Mehrabani, S.; Bagheri, R.; Song, Z.; Shen, J. R.; Allakhverdiev, S. I. An Aluminum/Cobalt/Iron/Nickel Alloy as a Precatalyst for Water Oxidation. *Int. J. Hydrogen Energy* **2018**, *43* (4), 2083–2090. https://doi.org/10.1016/j.ijhydene.2017.12.025.

(55) Carrasco, J.; Lõpez-Durán, D.; Liu, Z.; Duchoň, T.; Evans, J.; Senanayake, S. D.; Crumlin, E. J.; Matolín, V.; Rodríguez, J. A.; Ganduglia-Pirovano, M. V. In Situ and Theoretical Studies for the Dissociation of Water on an Active Ni/CeO2 Catalyst: Importance of Strong Metal-Support Interactions for the Cleavage of O-H Bonds. *Angew. Chemie - Int. Ed.* **2015**, *54* (13), 3917–3921. https://doi.org/10.1002/anie.201410697.

(56) Wagner, M.; Lackner, P.; Seiler, S.; Brunsch, A.; Bliem, R.; Gerhold, S.; Wang, Z.; Osiecki, J.; Schulte, K.; Boatner, L. A.; Schmid, M.; Meyer, B.; Diebold, U. Resolving the Structure of a Well-Ordered Hydroxyl Overlayer on In2O3(111): Nanomanipulation and Theory. *ACS Nano* **2017**, *11* (11), 11531–11541. https://doi.org/10.1021/acsnano.7b06387.

(57) Boaro, M.; Giordano, F.; Recchia, S.; Santo, V. D.; Giona, M.; Trovarelli, A. On the Mechanism of Fast Oxygen Storage and Release in Ceria-Zirconia Model Catalysts. *Appl. Catal. B Environ.* **2004**, *52* (3), 225–237. https://doi.org/10.1016/j.apcatb.2004.03.021.

(58) Biesinger, M. C.; Payne, B. P.; Lau, L. W. M.; Gerson, A.; Smart, R. S. C. X-Ray Photoelectron Spectroscopic Chemical State Quantification of Mixed Nickel Metal, Oxide and Hydroxide Systems. *Surf. Interface Anal.* **2009**, *41* (4), 324–332. https://doi.org/10.1002/sia.3026.

(59) Shih, S. J.; Chang, L. Y. S.; Chen, C. Y.; Borisenko, K. B.; Cockayne, D. J. H. Nanoscale Yttrium Distribution in Yttrium-Doped Ceria Powder. *J. Nanoparticle Res.* **2009**, *11* (8), 2145–2152. https://doi.org/10.1007/s11051-009-9585-2.

(60) Atribak, I.; Bueno-López, A.; García-García, A. Role of Yttrium Loading in the Physico-Chemical Properties and Soot Combustion Activity of Ceria and Ceria-Zirconia Catalysts.

J. Mol. Catal. A Chem. **2009**, *300* (1–2), 103–110. https://doi.org/10.1016/j.molcata.2008.10.043.

(61) Shih, S. J.; Wu, Y. Y.; Borisenko, K. B. Control of Morphology and Dopant Distribution in Yttrium-Doped Ceria Nanoparticles. *J. Nanoparticle Res.* **2011**, *13* (12), 7021–7028. https://doi.org/10.1007/s11051-011-0614-6.

(62) Shih, S. J.; Li, G.; Cockayne, D. J. H.; Borisenko, K. B. Mechanism of Dopant Distribution: An Example of Nickel-Doped Ceria Nanoparticles. *Scr. Mater.* **2009**, *61* (8), 832–835. https://doi.org/10.1016/j.scriptamat.2009.07.008.

(63) Kugai, J.; Subramani, V.; Song, C.; Engelhard, M. H.; Chin, Y. H. Effects of Nanocrystalline CeO2 Supports on the Properties and Performance of Ni-Rh Bimetallic Catalyst for Oxidative Steam Reforming of Ethanol. *J. Catal.* **2006**, *238* (2), 430–440. https://doi.org/10.1016/j.jcat.2006.01.001.

(64) Ashok, J.; Ang, M. L.; Terence, P. Z. L.; Kawi, S. Promotion of the Water-Gas-Shift Reaction by Nickel Hydroxyl Species in Partially Reduced Nickel-Containing Phyllosilicate Catalysts. *ChemCatChem* **2016**, *8* (7), 1308–1318. https://doi.org/10.1002/cctc.201501284.

(65) Xue, L.; Zhang, C.; He, H.; Teraoka, Y. Catalytic Decomposition of N2O over CeO2 Promoted Co3O4 Spinel Catalyst. *Appl. Catal. B Environ.* **2007**, *75*, 167–174. https://doi.org/10.1016/j.apcatb.2007.04.013.

(66) Bellido, J. D. A.; Assaf, E. M. Effect of the Y2O3-ZrO2 Support Composition on Nickel Catalyst Evaluated in Dry Reforming of Methane. *Appl. Catal. A Gen.* **2009**, *352*, 179–187.

(67) Italiano, C.; Llorca, J.; Pino, L.; Ferraro, M.; Antonucci, V.; Vita, A. CO and CO2 Methanation over Ni Catalysts Supported on CeO2, Al2O3 and Y2O3 Oxides. *Appl. Catal. B Environ.* **2020**, *264*, 118494. https://doi.org/10.1016/j.apcatb.2019.118494.

(68) Sun, C.; Beaunier, P.; Da Costa, P. Effect of Ceria Promotion on the Catalytic Performance

of Ni/SBA-16 Catalysts for CO2 Methanation. *Catal. Sci. Technol.* **2020**, *10*, 6330–6341. https://doi.org/10.1039/d0cy00922a.

(69) Ashok, J.; Ang, M. L.; Kawi, S. Enhanced Activity of CO2 Methanation over Ni/CeO2-ZrO2 Catalysts: Influence of Preparation Methods. *Catal. Today* **2017**, *281*, 304–311. https://doi.org/10.1016/j.cattod.2016.07.020.

(70) Lee, S. M.; Lee, Y. H.; Moon, D. H.; Ahn, J. Y.; Nguyen, D. D.; Chang, S. W.; Kim, S. S. Reaction Mechanism and Catalytic Impact of Ni/CeO2-x Catalyst for Low-Temperature CO2 Methanation. *Ind. Eng. Chem. Res.* **2019**, *58*, 8656−8662. https://doi.org/10.1021/acs.iecr.9b00983.

Highlights

- Ni (5wt%) was deposited over Y-modified CeO_2 oxides prepared by hydrothermal method.
- Y promotion tailored the particle sizes and shapes of CeO_2 in the Ni catalysts.
- The oxygen vacancies activated CO_2 promoting the CO_2 methanation catalytic activity.
- Ni particles well dispersed on CeO_2-Y oxides provided active sites for H_2 dissociation
- Ni/CeO_2-Y 2.0% exhibited the highest CO_2 conversion and high CH_4 selectivity.